Turbulent flow structure across the spanwise edge of a canopy model

Ewelina Winiarska · Roni Goldshmid ·
Dan Liberzon · René van Hout

Abstract
The turbulent flow field over a spanwise-heterogeneous vegetative canopy model was investigated to examine the impact of heterogeneity on energy and momentum transport processes. Constant temperature anemometry, paired with a novel Deep Learning-based calibration methodology, enabled high-resolution measurements of velocity components and turbulent kinetic energy (TKE) spectra, spanning several orders of magnitude and resolving dissipation scales. A controlled experimental framework facilitated the collection of multi-point, high-frequency turbulence statistics, capturing the intricate flow dynamics across canopy and open patch regions. In the homogeneous configuration, velocity profiles exhibited minimal variation across spanwise positions, with turbulence intensity peaking near the canopy height, where aerodynamic drag enhanced energy dissipation. Spectral analysis revealed distinct inertial and dissipation ranges, indicating the presence of robust turbulent structures that drive the energy cascade. In the heterogeneous layout, the boundary layer flow transitioned distinctly across the open patch, resembling rough plate behavior. Near canopy edges, elevated turbulence intensity, and TKE signaled strong interactions between vegetation and airflow, while TKE sharply diminished

E. Winiarska
Department of Earth and Planetary Sciences, Weizmann Institute of Science, 7610001, Rehovot, Israel. E-mail: ewelina.winiarska@weizmann.ac.il

R. Goldshmid
Department of Aerospace Engineering, San Diego State University, San Diego, CA 92115, USA.

D. Liberzon
Faculty of Civil and Environmental Engineering, Technion - Israel Institute of Technology, 3200003 Haifa, Israel.

R. van Hout
Faculty of Mechanical Engineering, Technion - Israel Institute of Technology, 3200003 Haifa, Israel. E-mail: rene@technion.ac.il

deeper into the open patch. Variations in turbulence length scales, particularly Taylor and horizontal integral scales, highlighted the role of heterogeneity in modulating atmospheric boundary layer dynamics. These findings provide insights into how spanwise heterogeneity influences turbulent energy redistribution and flow characteristics. The results contribute to a better understanding of canopy-atmosphere interactions and may support the refinement of models used for predicting wind flow and transport phenomena in heterogeneous environments.

1 Introduction

Earth's land surface encompasses diverse environments, including deserts, urban structures, and vegetation-covered regions. Among these, plant canopies, spanning both agricultural fields and natural ecosystems, are particularly significant due to their vast coverage and central role in mediating exchanges of momentum, heat, and mass between the atmosphere and the biosphere (Patton et al. 2016; Vilà-Guerau de Arellano et al. 2023). These interactions profoundly influence climatic processes across a wide range of scales, making plant canopies a focal point for understanding atmospheric turbulence. Understanding turbulent flow in the plant environment is primarily driven by the desire to comprehend these transport mechanisms resulting from the dynamic interaction between the airflow and vegetation elements, which occur over a broad spectrum of temporal and spatial scales (see e.g. Kaimal and Finnigan 1994; Poggi et al. 2004; Finnigan et al. 2009). Despite substantial progress, capturing the full complexity of these interactions remains an ongoing scientific challenge, with implications for ecological modeling and environmental management (Katul et al. 2012; Bonan et al. 2018).
Over the past few decades, research has considerably advanced our understanding of turbulent flows over homogeneous plant canopies, characterized by their minimal variation in height or density. Extensive experimental evidence gathered from laboratory experiments (Seginer et al. 1976; Raupach et al. 1986; Brunet et al. 1994; Ghisalberti and Nepf 2002) and *in situ* (Shaw et al. 1974; Brunet et al. 1992; Gao et al. 1989; Thomas and Foken 2007; Zhu et al. 2007), has led to the emergence of a remarkably consistent picture, in which turbulence within and just above homogeneous vegetation canopies is largely characterized by intermittent and energetic coherent structures, typically exhibiting length scales comparable to the height of the canopy (Raupach and Thom 1981; Finnigan 2000; Brunet 2020). While these studies offer foundational insights, the pronounced spatial variability found in natural and agricultural ecosystems highlights the need to extend this understanding to heterogeneous canopies.
In natural ecosystems, heterogeneity is the rule rather than the exception.

Even agricultural fields, designed for efficiency and uniformity, often feature abrupt transitions between crop-covered and open areas, introducing variability at multiple spatial scales. Field observations and modeling efforts have demonstrated that vegetation discontinuities across these interfaces can significantly alter turbulence and boundary layer dynamics. For example, contrasts in TKE production and dissipation have been reported across forest-scrubland transitions in semi-arid landscapes (Banerjee et al. 2018), and canopy-edge studies have shown that isolated forest patches can modulate boundary layer depth and turbulent structure through surface–atmosphere coupling (Kröniger et al. 2018; Brugger et al. 2018). Laboratory experiments further indicate that vegetation edges induce localized flow reorganization through strong velocity and pressure gradients at canopy inlets, leading to momentum redistribution within the entry region (Moltchanov et al. 2015). Accounting for canopy heterogeneity in models presents significant challenges, due to the wide range of spatial scales involved, from the shape of individual plants to gaps and patches on the order of the canopy boundary layer height (Bou-Zeid et al. 2007, 2020). Prior research has thoroughly explored how abrupt changes in surface roughness along interfaces, aligned either perpendicular or parallel to the prevailing surface wind direction, can lead to the development of internal boundary layers (Antonia and Luxton 1972; Garratt 1990) or the initiation of secondary flow circulations (Anderson et al. 2015; Vanderwel and Ganapathisubramani 2015). However, notable gaps remain in understanding turbulence structure, momentum, and energy exchange, especially concerning spanwise heterogeneity. Traditionally, most studies have focused on scenarios where prevailing winds are perpendicular to landscape variations, resulting in the formation of an internal boundary layer (Belcher et al. 2003; Cheng and Castro 2002; Dupont and Brunet 2009). In contrast, relatively little attention has been directed toward cases where prevailing winds are parallel to landscape heterogeneity, a regime referred to as "spanwise heterogeneity" (Brutsaert 1998; Grant 1991; Bou-Zeid et al. 2004; Winiarska et al. 2023, 2024). Recent large-eddy simulations by Joshi and Anderson (2022) demonstrate that even modest spanwise variations in canopy roughness can markedly reorganize near-canopy turbulence and enhance momentum exchange, underscoring the need for a deeper understanding of heterogeneity-driven turbulent flow structures. Related studies have also shown that large and persistent circulations in the atmospheric boundary layer (ABL) can form under weak prevailing flows (Omidvar et al. 2020) or when the mean velocity direction aligns parallel to interfaces between different patches (Raasch and Harbusch 2001). Studies on these secondary flows have primarily focused on streamwise-aligned rib-like surfaces, demonstrating significant spanwise wall-normal secondary flows (Anderson et al. 2015; Chung et al. 2018; Vanderwel et al. 2019; Medjnoun et al. 2018). Conversely, research investigating the impact of spanwise heterogeneity on turbulent flow characteristics, relevant to vegetative canopies, has predominantly focused on water flow environments such as vegetated riverbanks, floodplains, and estuarine channels with fringing mangroves (e.g., Li et al. 2022; Nezu and Onitsuka 2002; White and Nepf 2008; Yan et al. 2016; Unigarro Villota et al. 2023), where vegetation

emerges from the water. Research in these settings has shown that transverse velocity inflection points near vegetation edges generate coherent vortices, significantly enhancing momentum exchange across the spanwise edge.

The fine structure of turbulence is often characterized through the spectral distribution of velocity fluctuations, which has been extensively examined in horizontally homogeneous canopies. Foundational studies in corn fields (Shaw et al. 1974; Wilson et al. 1982), forest canopies (Amiro 1990), and wind tunnel models using hot-wire anemometry (Seginer et al. 1976; Raupach et al. 1986; Brunet et al. 1994) have established key spectral features associated with canopy-layer turbulence. Building on this foundation, recent studies have explored how canopy structure influences turbulent velocity field spectra. Freire et al. (2023) documented deviations from the classical inertial-range scaling in orchard canopies, including a pronounced high-frequency spectral bottleneck, highlighting how vegetation-induced constraints can alter the energy distribution. Mao et al. (2024) found that canopy density modulates dominant spectral modes, shifting the energy peaks associated with shear-layer instabilities and wake eddies. While informative, these findings are largely confined to vertically stratified or streamwise-aligned configurations. The present study extends this perspective by investigating how spanwise canopy heterogeneity affects the energy distribution across turbulence scales, an aspect rarely addressed in existing spectral analyses.

Yet despite these insights, a comprehensive understanding remains lacking regarding the mechanisms governing flow-vegetation interactions and their impact on TKE cascades, spectral shapes, and turbulent length scales near spanwise vegetative edges. Building upon our recent efforts investigating turbulent transport mechanisms at spanwise canopy edges (Winiarska et al. 2023, 2024), we employed a large atmospheric boundary layer (ABL) wind tunnel to examine turbulent wind flow characteristics and evaporation processes within and above a vegetative canopy model designed to replicate the aerodynamic properties of a mature corn canopy. These investigations used stereoscopic particle image velocimetry (SPIV) and in-house-designed evaporation probes. SPIV was employed to acquire a detailed, spatially resolved, 3D instantaneous velocity field within and just above the canopy model, in particular focusing on the local field characteristics (micro-scale) and spanwise turbulent transport across spanwise vegetative canopy edges (Winiarska et al. 2023). The SPIV measurements were not time-resolved, and the field of view only spanned a small part of the canopy.

To address these limitations, in the current study, we employ constant temperature anemometry (CTA) as the primary sensing method, paired with a novel Deep Learning-based calibration methodology (Goldshmid et al. 2022). This combination provides high temporal resolution, enabling the precise characterization of turbulence features with unmatched accuracy, even under the demanding conditions of high-intensity turbulence. It allows for accurate measurement of mean and fluctuating velocity components across several orders of magnitude, while fully resolving the spectrum of turbulent fluctuation scales (Bruun 1996). By acquiring multi-point, high-frequency turbulence statistics,

this study enables an in-depth analysis of spanwise heterogeneity influences on the mean flow properties, TKE spectral organization, and TKE dissipation dynamics.

Insights from this research are expected to support the development of more accurate models for predicting canopy-atmosphere interactions, which is crucial for applications in ecosystem management, precision agriculture, and climate modeling. By incorporating the effects of spanwise heterogeneity, these models can better inform strategies for sustainable land use and environmental conservation. The experimental setup, including the description of the wind tunnel, model canopy, CTA calibration, data acquisition, and processing, is detailed in Section 2. The results are presented in Section 3, with concluding remarks in Section 4.

2 Experimental setup

2.1 Wind tunnel and canopy model

The experiments were conducted in the Technion-IIT's Environmental Wind Tunnel, featuring a 16.1 m long test section with cross-section dimensions of 1.95×1.95 m^2. The tunnel operates in an open-circuit flow-suction mode and maintains a negligible streamwise pressure gradient via an adjustable roof profile. An ABL is generated through a transverse array of four elliptic wedge vortex generators and a downstream wire mesh to induce shear and turbulence. To increase surface roughness, gravel is spread across the tunnel floor. Detailed specifications of the tunnel can be found in Winiarska et al. (2023). Within the wind tunnel, a model canopy with a length of 4.8 m was assembled. This canopy consists of triangular-shaped elements with a height of $h = 200$ mm, perforated with 18 and 20-mm diameter holes distributed over three levels. The canopy layout is configured in an inline arrangement, perpendicular to the streamwise velocity component, with a streamwise spacing of 10 ±0.5cm. Canopy elements are mounted on base strips, each accommodating 4 to 5 elements (see Fig. 1a). The design mimics the vertical distribution of the projected frontal area index (PFAI), defined as the total frontal area of the canopy elements projected onto a plane normal to the flow direction, per unit ground area. This arrangement yields a PFAI of 0.61. While lower than for typical maize crops, this density remains characteristic of relatively dense artificial vegetative canopies (see e.g. Shaw et al. 1974; Wilson et al. 1982; Finnigan 2000; van Hout et al. 2007; Zhu et al. 2006). All the experiments were conducted in both homogeneous and heterogeneous canopy layouts, as detailed by Winiarska et al. (2023). To introduce spanwise heterogeneity, the homogeneous layout was changed by removing the canopy elements highlighted in red (see Fig. 1a), thus creating a 63 cm wide open patch in the middle section of the canopy model. A right-handed Cartesian coordinate system, x_i, where $i = 1, 2$, and 3 denote the streamwise, spanwise, and wall-normal directions, was employed (see Fig. 1). The origin is positioned at location 7 and projected onto the bottom wall as shown in Fig. 1. Corresponding instantaneous flow velocities are denoted by U_i, fluctuating velocity components (Reynolds decomposed) by u_i ($i = 1$ to 3). Ensemble-averaged values, denoted by an overbar, were calculated as averages over time series measurements at each height. Spatial averages are denoted by the chevrons "$\langle \quad \rangle$".

     Within the wider scope of this project, the three components of the instantaneous velocity field across the spanwise canopy edge, within, and above the heterogeneous as well as the homogeneous canopy layout were measured using SPIV and CTA. SPIV measurements reported by Winiarska et al. (2023) and Winiarska et al. (2024) were followed by hot-wire measurements in CTA operational mode. The SPIV measurements were performed 3.3 m ($16.5h$) downstream of the start of the model canopy (Fig. 1a), where the mean flow was fully developed as determined by preliminary measurements made by scanning the developing flow field along the test section by an array of Pitot tubes. The

SPIV's field of view (FOV) covered approximately 13×13 cm^2, and a detailed description of the setup and the measurements can be found in Winiarska et al. (2023) and Winiarska et al. (2024). The CTA measurements were performed at one streamwise position, 3.335 m ($16.675h$) from the start of the canopy model. In total, CTA measurements were conducted at 179 different locations as illustrated by the black and red dots in Fig. 1b that indicate the positions at which the CTA measurements were performed in the homogeneous (only black dots, 144 locations) and the heterogeneous (black and red dots, 179 locations) layouts. In the spanwise direction, 12 points were visited (Fig. 1). Locations 2, 4, 9, and 11 were aligned with the middle of the canopy elements (see Fig. 1c) while locations 3, 5, 8, 10, and 12 were positioned in the middle of the gap between the canopy elements. Locations 6, 7, and 8 were selected to examine gradients across the canopy edge and clear patch transition. Note that location 1 was positioned at the edge of the canopy element because of technical limitations. In the wall-normal direction above the canopy, CTA measurements were conducted at 12 points. The point closest to the canopy was $x_3/h = 1.03$ and points higher than that were logarithmically evenly spaced at $x_3/h = 1.03, 1.06, 1.09, 1.13, 1.17, 1.23, 1.27, 1.35, 1.46, 1.6, 1.78, 2.03$ in locations above the elements and the gaps for both the homogeneous and heterogeneous setups. Below canopy height, in the open patch for the heterogeneous layout (red dots), an additional 7 points were visited at wall-normal positions of $x_3/h = 0.43, 0.65, 0.8, 0.9, 0.95, 0.98$, and 1.0. Note that locations 6, 7, and 8 coincided with the SPIV measurements for heights $x_3/h = 0.8, 0.9, 0.95$, and 1.0, enabling cross-validation. Velocity field measurements were conducted at three different flow rates, denoted hereafter by the corresponding free stream air velocities, $U_\infty = 3$, 5, and 6.8 m/s. The normalized 99% boundary layer thickness was $\delta/h = 3.5$, with $\delta = 0.70$ m based on Pitot tube measurements (not shown here). The corresponding boundary layer Reynolds number, defined as $Re_\delta = U_\infty \delta/\nu$ (with air kinematic viscosity $\nu = 1.5 \times 10^{-5}$ m^2/s), were $Re_\delta = 1.4 \times 10^5$, 2.3×10^5, and 3.2×10^5 for $U_\infty = 3$, 5, and 6.8 m/s, respectively.

2.2 CTA calibration and data acquisition

The CTA measurements were conducted using two co-located X-shaped hot-wire probes (1241-20 X-probes, Thermo Systems), each wire sensor was operated by a dedicated CTA channel (Dantec Dynamics). Each X-probe captures two instantaneous velocity components, with one probe providing the U_1 and U_2 components, while the other provides the U_1 and U_3 components, as they are oriented at 90 degrees in the roll axis relative to each other (e.g Goldshmid et al. 2022; Kit et al. 2010). The U_1 components measured by both probes are averaged, effectively enhancing the signal-to-noise ratio. A similar multi-sensor strategy was successfully applied in field conditions using a sonic–hot-film setup to extract turbulence statistics in thermally driven slope flows (Hilel Goldshmid and Liberzon 2020). Note that the two X-shaped sen-
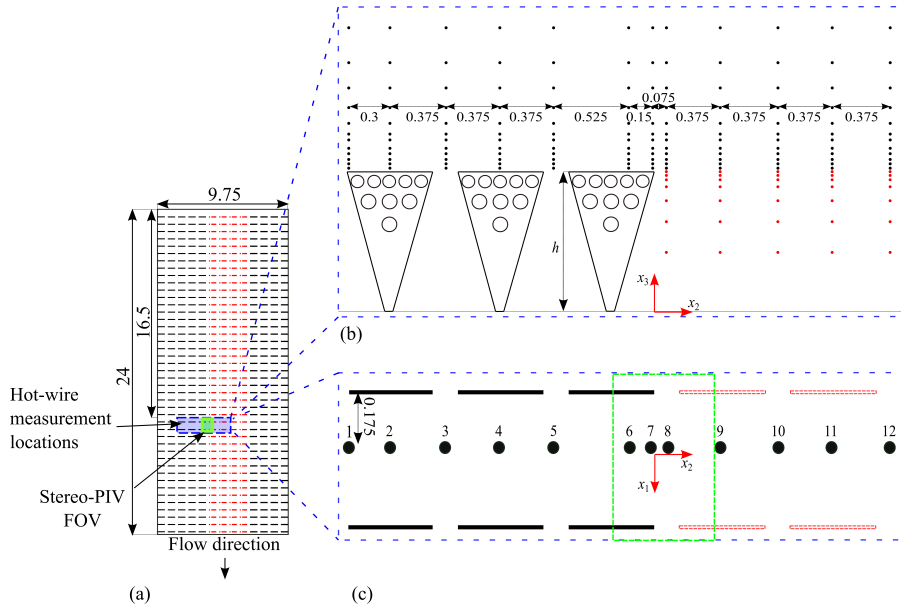
Fig. 1 (a) Illustration of the homogeneous, and spanwise heterogeneous (canopy elements in red were removed in the latter configuration) model canopy layouts in the wind tunnel. The SPIV's FOV is marked by a green square located 3.3 m ($16.5h$) downstream of the start of the model canopy. The blue-highlighted section indicates the region perpendicular to the streamwise direction along which the CTA measurements were taken. (b) Zoomed-in cross-sectional view illustrating 144 measurement points in a homogeneous setup (black dots), and 144 (black dots) plus 35 (red dots) in the heterogeneous layout; (c) Zoomed-in top view of canopy elements and the 12 positions (in the transverse direction) at which CTA measurements were performed. CTA measurements were conducted at one streamwise position, 3.335 m ($16.675h$) from the start of the canopy model. Distances are normalized by h.

sors are separated by 1.8 mm, which defines the effective spatial resolution of the probe. Although using dual X-shaped probes slightly reduces spatial resolution compared to a single triple-wire probe, it significantly improves the signal-to-noise ratio (Kit and Liberzon 2016). CTA calibration was performed using an automated calibration system (StreamLine Pro Automatic Calibrator, Dantec Dynamics) consisting of a well-defined jet flow with a motorized pitch and yaw manipulator. An overheat ratio of 0.8 (1.8 times the flow temperature), resulting in a mean wire temperature of approximately 240°C, was maintained for all sensors during both calibration and actual tunnel measurements. During the calibration, the probe was positioned at the jet mouth, and the flow velocity and probe orientation were systematically varied across a parameter range of interest, determined by the anticipated flow conditions. The range was predetermined to adhere to the mean flow orientation variations at the probe due to the expected variations in mean flow and TI during the actual measurements (van Dijk and Nieuwstadt 2004; Kit et al. 2010; Kit and Liberzon 2016). Data collection and processing were performed using a

specially written MATLAB® routine. Preliminary tests, including Pitot tube scans of velocity profiles above the canopy and previous results from the SPIV measurements, were used to determine the optimal calibration settings. The calibration parameters encompassed 28 distinct mean jet velocities (in a range between 0 m/s and 10 m/s) and 225 angles of attack relative to the main jet axis (forming a wide cone covering changes in azimuth and elevation in the range between -45.5° and +45.5° with increments of 6.5° on each axis) at each mean velocity, resulting in a total of 6500 unique calibration points. At each point, the voltages from all four sensors were sampled for five seconds at 6 kHz and then averaged. The corresponding mean jet velocity was decomposed into three orthogonal components in the coordinate system aligned with the probe, at each of the 225 angles of attack. The voltages and the three velocity component values constituted the calibration set, and a Deep Neural Network was trained on this set as described in Goldshmid et al. (2022). The trained network constituted the transform voltage-to-velocity function to convert the voltages recorded during the measurements. The Deep Learning-based calibration was demonstrated to be preferable compared to the traditional polynomial fit and lookup table methodologies, as it provides similar accuracy while allowing calibration for an extensive range of mean velocities and angle of attack (due to the expected high turbulence intensity (TI) of the flow). Following calibration, the probe system was transferred to the wind tunnel, mounted on a rigid aluminum frame aligned using a cross-line laser level. The frame was connected to a PC-controlled 3D traverse system with encoder-based precision and laser range finders, supporting vertical positioning within ±0.5 mm accuracy. The above-mentioned wide range of jet velocities and angles of attack resulted in a long calibration taking a few hours. Hence, the traditionally implemented routine of pre- and post-measurement calibration was impractical, and to ensure the reliability of the recorded data, the probe was left in the wind tunnel continuously during each part of the measurement campaign, which lasted several days. Instead of daily recalibration, the calibration was re-validated daily by re-measuring the velocities at the last visited measurement position and flow conditions. This routine was repeated until at least one hot-wire was burned or produced erroneous results, rendering the previous calibration invalid, necessitating re-calibration. Throughout the measurement runs, ambient conditions such as temperature and relative humidity were continuously monitored and kept constant through the readjustment of the air conditioning system. Throughout the several-month experimental campaign, temperature variations were maintained within ±0.5°C, and relative humidity fluctuations were kept below ±3%. The measurement uncertainties for RH and temperature were ±1% and ±0.4°C, respectively. All the data acquisition, including the monitoring of ambient conditions, was performed via in-house developed LabVIEW® and MATLAB® routines.

2.3 Methods and Data Processing

Time series of the three components of the velocity field were acquired using the CTA system, sampled at 6 kHz to resolve fluctuations down to the Kolmogorov scale. At each measurement location, data were recorded continuously for 120 s, yielding statistically converged time series with high spectral resolution. A digital low-pass filter with a cutoff frequency of 1890 Hz was applied during post-processing to suppress high-frequency (near 2 kHz) noise from the motion-control system.

The instantaneous velocity field components fluctuations $u_1(t)$, $u_2(t)$, and $u_3(t)$, corresponding to the streamwise, spanwise, and vertical directions respectively, were analyzed through their power spectral densities $S_{ii}(f)$. Spectra were computed using the Fast Fourier Transform (FFT) with non-overlapping averaging windows of 1, 5, and 10 seconds, with no additional windowing function applied. While the spectral shapes were broadly consistent across these durations, the 1-second averaging windows yielded the smoothest and most stable spectral shapes, while preserving essential broadband energy-cascade characteristics (see Fig. S1, Supplementary Material). Consequently, all spectral analyses presented in this study employ 1-second, non-overlapping averaging windows, with a resulting frequency resolution of 1 Hz.

The spectral analysis relies explicitly on Kolmogorov's hypothesis of locally isotropic turbulence and Taylor's frozen turbulence hypothesis, which relates temporal frequency f to spatial wavenumber k_1 via, $k_1 = \frac{2\pi f}{\overline{U}_1}$, where $\overline{U}_1$ is the local mean streamwise velocity. Within the inertial subrange (ISR), the spectra are expected to follow a characteristic $f^{-5/3}$ scaling. Kolmogorov's isotropy assumption additionally implies a fixed spectral relationship within the ISR: $S_{33}(f) = S_{22}(f) = \frac{4}{3}S_{11}(f)$. To examine and quantify departures from ideal ISR scaling and isotropy, compensated spectra were computed as:

$$\frac{k_1^{5/3} S_{ii}(f)}{\epsilon^{2/3}}, \tag{1}$$

where ϵ is the TKE dissipation rate. Spectra were further evaluated using the dimensionless wavenumber $k_1\eta$, defined through the Kolmogorov length scale:

$$\eta = \left(\frac{\nu^3}{\epsilon}\right)^{1/4}. \tag{2}$$

The turbulent kinetic energy is defined as:

$$\text{TKE} = \frac{\overline{u_1^2 + u_2^2 + u_3^2}}{2}. \tag{3}$$

The dissipation rate ϵ was estimated from velocity time derivatives, assuming local isotropy at small scales. While the assumption of isotropy does not strictly hold in canopy flows, particularly near the canopy top where shear and spatial heterogeneity are pronounced, Kolmogorov's similarity hypothesis predicts that velocity-gradient statistics tend toward so-called local isotropy

as scales decrease, even in strongly anisotropic environments (Pope 2001). Beginning from the isotropic TKE dissipation rate tensor:

$$\epsilon = 2\nu\overline{s_{ij}s_{ij}}, \quad \text{with} \quad s_{ij} = \frac{1}{2}\left(\frac{\partial u_i}{\partial x_j} + \frac{\partial u_j}{\partial x_i}\right), \tag{4}$$

and invoking Taylor's hypothesis ($\partial/\partial x_1 \approx (1/\overline{U}_1)\,\partial/\partial t$), directional dissipation rates reduce to:

$$\epsilon_{11} = 15\nu\frac{\overline{(\partial u_1/\partial t)^2}}{\overline{U}_1^2}, \quad \epsilon_{22} = 7.5\nu\frac{\overline{(\partial u_2/\partial t)^2}}{\overline{U}_1^2}, \quad \epsilon_{33} = 7.5\nu\frac{\overline{(\partial u_3/\partial t)^2}}{\overline{U}_1^2}, \tag{5}$$

with the mean dissipation rate defined as:

$$\epsilon = (\epsilon_{11} + \epsilon_{22} + \epsilon_{33})/3. \tag{6}$$

By computing dissipation rates independently from the spectra using Eq. 5, we avoid circular normalization, thus directly assessing how spectra collapse across regions of varying canopy structure. A similar time-resolved dissipation approach was applied by van Hout et al. (2007), albeit their field study utilized spatial PIV measurements instead of hot-wire temporal derivatives. This mean dissipation rate (Eq. 6) was applied uniformly across spectral normalizations. However, to assess the observed anisotropy and directional deviations from ideal ISR behavior, empirical Kolmogorov constants were also evaluated component-wise. For each velocity component, the constant C_1 was defined as:

$$C_1^{(ii)} = \frac{k_1^{5/3}S_{ii}(f)}{\epsilon_{ii}^{2/3}}, \tag{7}$$

where ϵ_{ii} is the component-specific dissipation rate. Under conditions of local isotropy, the one-dimensional streamwise spectrum $S_{11}(k_1)$ is expected to follow Kolmogorov scaling with $C_1^{(11)} \approx 0.5$–0.6 (Pope 2001). Theoretical relationships further imply:

$$C_1^{(22)} = C_1^{(33)} = \frac{4}{3} \times C_1^{(11)} \approx 0.67\text{–}0.80, \tag{8}$$

consistent with experimental results from high-Reynolds-number turbulent boundary layers (Saddoughi and Veeravalli 1994). Deviations from these canonical values, either in magnitude or in spectral shape plateau behavior, may indicate the presence of local anisotropy, canopy-induced heterogeneity, Reynolds number effects, or breakdowns of the frozen-turbulence approximation. The empirical Kolmogorov constants $C_1^{(ii)}$ were determined from plateau levels of the measured compensated spectra. The one-dimensional energy spectra were computed independently per velocity component and height using non-overlapping 1-second segments for statistical convergence.

To further characterize the turbulence structure, length scales were also obtained from the velocity records. The Taylor microscale and the horizontal integral length scale were computed as:

$$\lambda = \sqrt{\frac{\overline{u_1^2}}{\overline{\left(\frac{1}{\overline{U_1}}\frac{\partial u_1}{\partial t}\right)^2}}},$$ (9)

and:

$$L_H = \frac{(\sqrt{\overline{u_1^2}})^3}{\epsilon},$$ (10)

respectively.

The analyses, including raw and compensated frequency-domain spectra, dissipation rates from velocity derivatives, empirical Kolmogorov constants, and the computed turbulence scales, form the basis for assessing deviations from classical ISR theory in the presence of canopy-induced heterogeneity. Results are presented and discussed in detail in the following sections.

3 Results and discussion

3.1 Validation

Prior to the actual hot-wire measurement campaign, the CTA measurements were validated by comparing the mean streamwise velocities to those obtained by the Pitot tubes and SPIV (see Fig. 2). While we observed some discrepancies in velocity magnitudes, the underlying trends remained consistent. Differences may be attributed to small variations in experimental conditions, partially the result of using a moving frame on which the Pitot tube and CTA were mounted. While the CTA was mounted 12 cm ($0.6h$) upstream of the frame, the Pitot tube was mounted only 3 cm ($0.15h$) upstream. In addition, the SPIV measurements were performed with the frame located 4 m ($20h$) downstream of the measurement position. The effect of the frame, together with small variations in experimental conditions and some misalignment of the canopy elements, likely contributed to the observed small discrepancies.

3.2 Mean velocity field

The analysis begins with the homogeneous canopy layout, which serves as a reference configuration for assessing the impact of spanwise heterogeneity. Example plots that display the measured averaged velocity components, $\overline{U}_1$, $\overline{U}_2$, and $\overline{U}_3$, normalized by the streamwise velocity component at canopy height, $\overline{U}_1^h$, are depicted in Fig. 3 at $U_\infty = 5$ m/s; similar trends were found at the other investigated velocities ($U_\infty = 3$ and 6.8 m/s). Note that values are taken
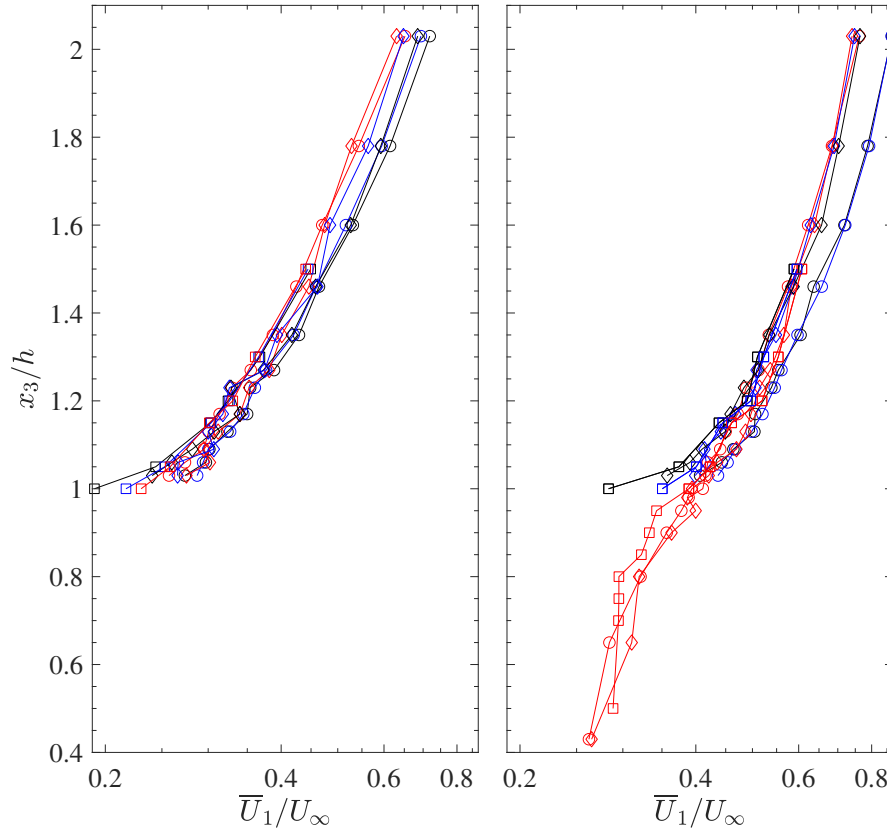
Fig. 2 Wall-normal profiles of the normalized, mean streamwise velocity ($\overline{U}_1/U_\infty$) at $x_1 = 3.335$ m ($16.675h$), measured at three transverse positions: 6 (black), 7 (blue), and 8 (red) at $U_\infty = 3$ m/s. Two layouts are considered: (a) Homogeneous layout, and (b) Heterogeneous layout. Hot-wire data (circle), Pitot tube data (diamond), and SPIV data (square).

at the canopy height $x_3/h = 1.03$, i.e., the lowest measurement point above the canopy elements.

The results depicted in Fig. 3 were divided into three "groups". The first group (G1), shown in the upper row of Fig. 3, includes positions 6, 7, and 8 (see Fig. 1), distributed across a single canopy element. It is shown that the normalized vertical profiles of the different velocity components exhibit similar shapes, and the variations across a single canopy element are small. The two other groups are comprised of positions in the middle of a canopy element (G2, positions 2, 4, 9, 11, middle row in Fig. 3) and those in the gap between two canopy elements (G3, positions 1, 3, 5, 8, 10, 12, bottom row in Fig. 3). Focusing on the profiles of $\overline{U}_1/\overline{U}_1^h$ (1st column in Fig. 3), it can be seen that, except for positions 1, 2, and 3, the profiles more or less collapse. Whereas the vertical profiles of $\overline{U}_1/\overline{U}_1^h$ show increase with increasing height, profiles of
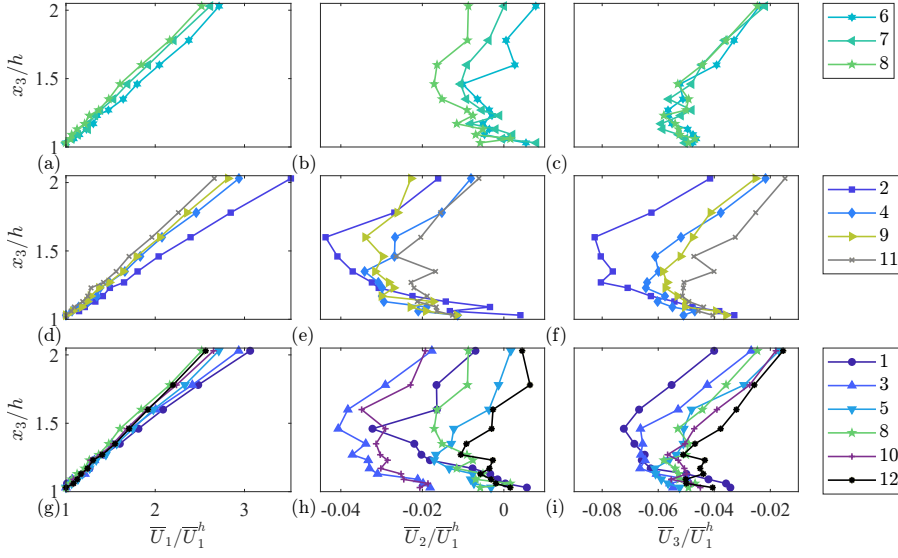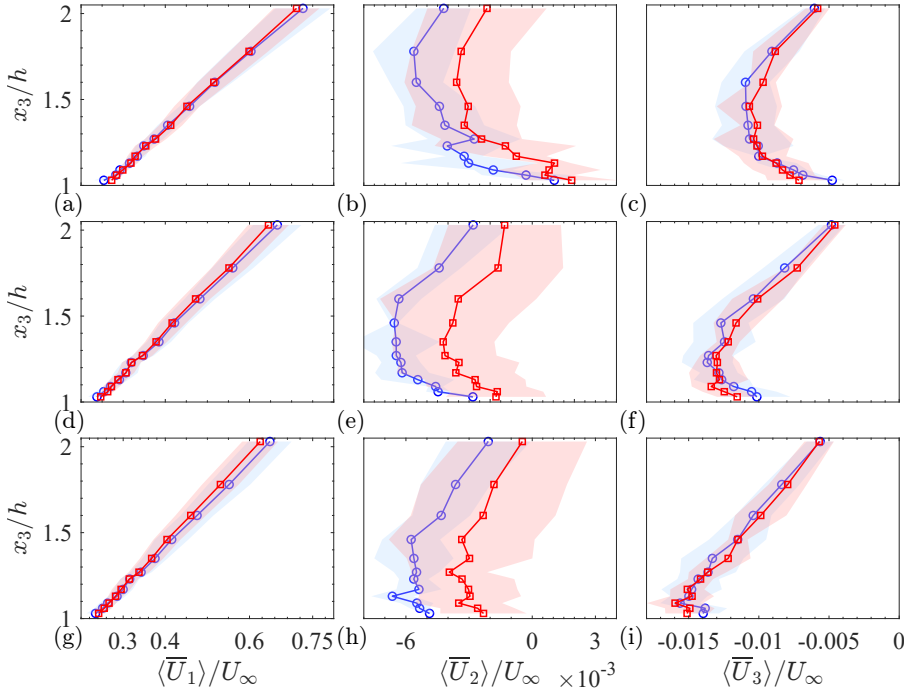
Fig. 3 Wall normal profiles of $\overline{U}_1/\overline{U}_1^h$ (1st column), $\overline{U}_2/\overline{U}_1^h$ (2nd column), $\overline{U}_3/\overline{U}_1^h$ (3rd column) at $U_\infty = 5$ m/s. 1st row: G1, 2nd row: G2, and 3rd row: G3. Numbers in the legend indicate measurement positions (see Fig. 1).
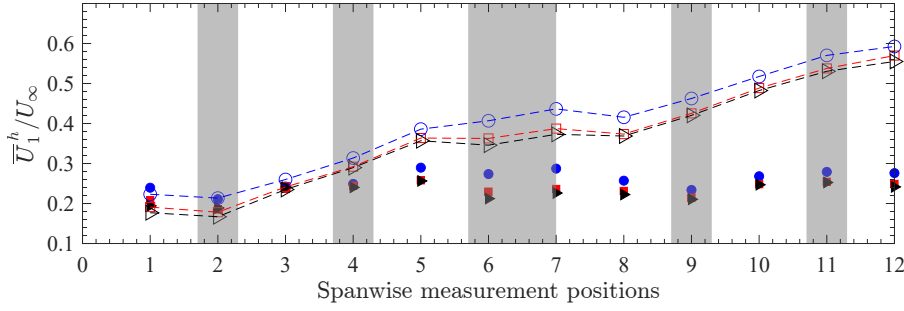
Fig. 4 Local values of mean streamwise velocity normalized by $U_\infty = 3$ m/s (blue symbols), 5 m/s (red symbols), and 6.8 m/s (black symbols) at $\frac{x_3}{h} = 1.03$ (canopy height) at the 12 spanwise measurement positions. Filled and open symbols correspond to the homogeneous and heterogeneous layouts, respectively. The gray shadings indicate canopy element obstructions.

$\overline{U}_2/\overline{U}_1^h$ (2nd column in Fig. 3) and $\overline{U}_3/\overline{U}_1^h$ (3rd column in Fig. 3) show peak magnitudes at about $x_3/h \approx 1.5$. Furthermore, in most cases, values of $\overline{U}_2/\overline{U}_1^h$ and $\overline{U}_3/\overline{U}_1^h$ are negative, reflecting downward and spanwise motions driven by canopy-induced turbulence. Note that positions 1–3, located near tunnel sidewalls, exhibit deviations likely caused by wall effects and are excluded from further analysis.

Figure 4 presents the spanwise variation of $\overline{U}_1^h/U_\infty$ for both the homogeneous (filled markers) and heterogeneous (open markers) canopy layouts across all
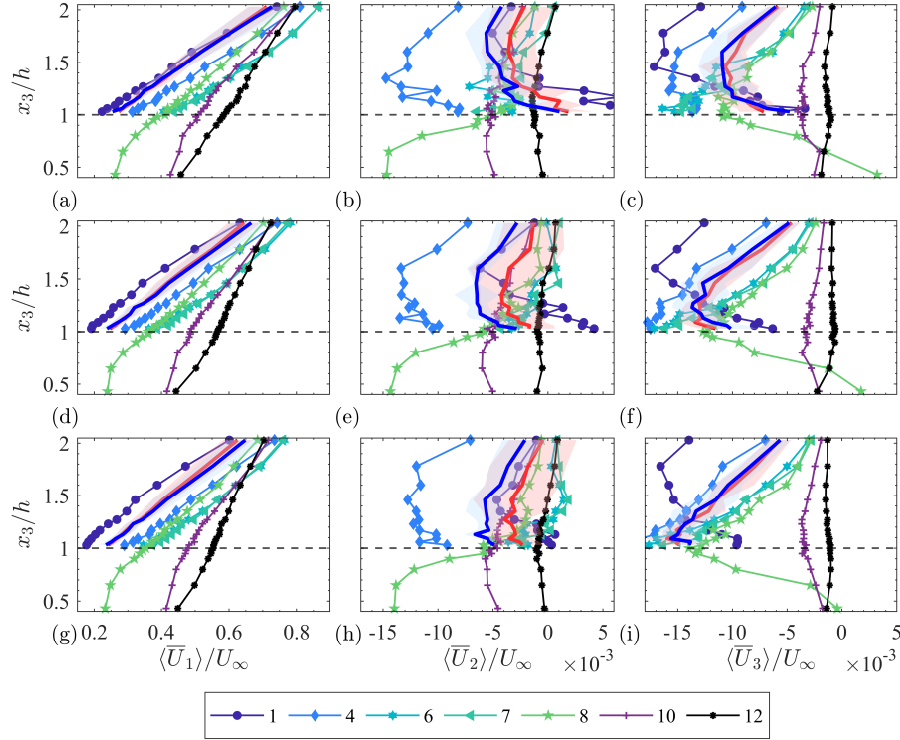
Fig. 5 Wall-normal profiles of $\langle \overline{U}_1 \rangle / U_\infty$ (1st column), $\langle \overline{U}_2 \rangle / U_\infty$ (2nd column), and $\langle \overline{U}_3 \rangle / U_\infty$ (3rd column). $U_\infty = 3$ m/s (1st row), 5 m/s (2nd row), and 6.8 m/s (3rd row). The blue and red profiles denote the average profiles for G2 and G3, respectively. The shaded areas indicate standard deviations of the profiles within G2 and G3.

tested free-stream velocities. In the homogeneous configuration, $\overline{U}_1^h / U_\infty$ is generally higher in the gaps between canopy elements compared to the regions directly above them (indicated by gray shading), consistent with flow channeling through unobstructed pathways. However, a local maximum in $\overline{U}_1^h / U_\infty$ is observed at position 7 near the canopy edge, rather than at position 8, the geometric center of the gap. This deviation from expected symmetric behavior may reflect minor inconsistencies in element placement or localized flow acceleration near the edge. In the heterogeneous layout, $\overline{U}_1^h / U_\infty$ exhibits a more gradual and monotonic increase in the spanwise direction as the flow enters the clear patch. Yet even here, position 7 consistently shows higher velocities than position 8, suggesting that flow does not immediately adjust to the unobstructed patch. These results suggest that localized acceleration near the canopy edge, likely resulting from enhanced shear or streamwise pressure gradients, is a robust feature present in both canopy configurations.

Figure 5 shows the group-averaged vertical profiles of the normalized velocity components, $\langle \overline{U}_i \rangle / U_\infty$ ($i = 1$–3), for groups G2 (blue) and G3 (red) across all tested U_∞. The profiles of $\langle \overline{U}_1 \rangle / U_\infty$ and $\langle \overline{U}_3 \rangle / U_\infty$ reveal minimal

differences between the groups, indicating negligible spanwise variability under
homogeneous canopy conditions. In contrast, the $\langle \overline{U}_2 \rangle / U_\infty$ profiles show slight
group-dependent differences that evolve with increasing U_∞, with the peak in
$\overline{U}_2$ gradually shifting toward the canopy height. Nevertheless, the magnitudes
of both $\overline{U}_2$ and $\overline{U}_3$ remain below a few percent of U_∞,
With the homogeneous case established as a reference, we now examine the
heterogeneous configuration. Figure 6 displays vertical profiles of normalized
velocity components at key positions spanning canopy elements (positions 1,
4, 6), the canopy edge (position 7), and the open patch (positions 8, 10, 12).
Each panel includes the red G3 average profile and standard deviation from
the homogeneous case for direct comparison.

Fig. 6 Wall-normal profiles of $\overline{U}_1/U_\infty$ (first column), $\overline{U}_2/U_\infty$ (second column), and $\overline{U}_3/U_\infty$
(third column) in the heterogeneous layout. Measurement locations are 1, 4, 6, 7, 8, 10, and
12. Each row corresponds to measurements taken at $U_\infty = 3, 5$, and 6.8 m/s. For comparison,
wall-normal profiles of spatially averaged $\langle \overline{U}_1 \rangle / U_\infty$, $\langle \overline{U}_2 \rangle / U_\infty$, and $\langle \overline{U}_3 \rangle / U_\infty$ for groups G2
and G3 in the homogeneous layout (see Fig. 5) are plotted in blue and red, respectively. The
shading represents the standard deviation. Horizontal dashed lines indicate canopy height.

The introduction of spanwise heterogeneity leads to clear and spatially
coherent deviations from the homogeneous baseline. At position 4, located
within the canopy, profiles of all velocity components begin to diverge from

those observed in the homogeneous case, suggesting that the effects of heterogeneity extend up to at least $1.05h$ from the canopy edge in the spanwise direction. This distance marks the onset of significant influence from lateral canopy structure, altering local flow dynamics relative to the previously uniform configuration. This divergence becomes more pronounced at positions 6 and 7, where the streamwise velocity component $\overline{U}_1/U_\infty$ increases substantially, nearly doubling relative to the homogeneous profile, highlighting strong acceleration near the canopy edge. In the adjacent clear patch (position 8), the influence of the nearby canopy edge remains evident: the $\overline{U}_1/U_\infty$ profile exhibits a shallow inflection point near $x_3/h \approx 1$, indicating persistent vertical shear associated with lateral flow adjustment at the canopy–open patch interface. Further into the clear patch, at positions 10 and 12, located approximately $0.45h$ and $0.825h$ from the canopy edge, the velocity profiles begin to resemble those of a canonical rough-wall boundary layer. The inflection point disappears, and the profile becomes smoother and more vertically uniform, indicating a diminishing canopy effect with increasing spanwise distance from the edge. The spanwise velocity component, $\overline{U}_2/U_\infty$, remains predominantly negative across most positions, with small positive values appearing near position 1 and close to the canopy top at lower U_∞. This trend reflects a progressive transition toward a unidirectional boundary layer flow, as both the spanwise ($\overline{U}_2$) and vertical ($\overline{U}_3$) velocity components diminish to near-zero levels deeper into the clear patch.

3.3 Turbulence structure

This section examines the structure of turbulence above and within the canopy by analyzing the TKE spectra, characteristic length scales, and inertial-range scaling. We begin by evaluating the spectral energy densities as well as the turbulence length scales to assess how energy is transferred across scales. This is followed by an analysis of turbulent kinetic energy dissipation rates and deviations from classical inertial-range scaling, which enables the assessment of the degree of anisotropy and the validity of isotropic turbulence assumptions in canopy-influenced flows.

3.3.1 Spectra

In the homogeneous configuration, power spectral density curves exhibit consistent shapes across all spanwise positions, allowing us to focus on a single representative location, position 12. Spectral densities for all three fluctuating velocity components and different free stream velocities ($U_\infty = 3, 5, 6.8$ m/s) are presented in Fig. 7. The results are shown in two vertical positions: near the canopy element ($x_3/h = 1.03$) and at a higher altitude ($x_3/h = 2.03$). Each column in the figure corresponds to a different free stream velocity. The spectral shapes and associated length scales, illustrated in Figs. 7, 8, 9, and 10 validate the ability of the here used CTA system to capture
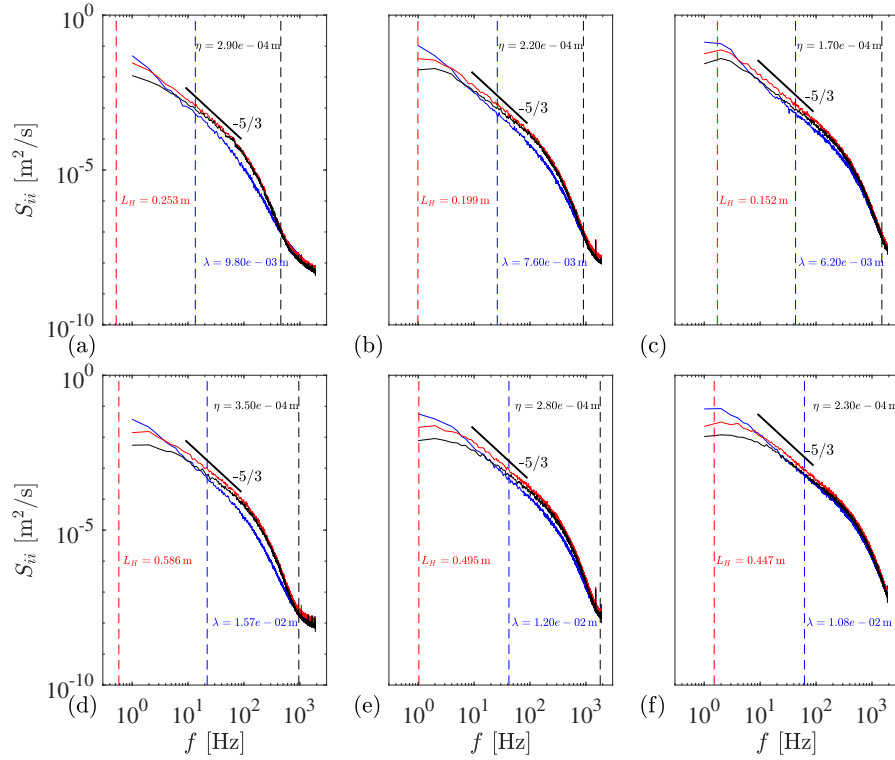
Fig. 7 Spectral analysis (position 12, homogeneous layout): power density spectra of fluctuating velocity components u_1 (blue), u_2 (red), and u_3 (black), measured at $U_\infty = 3$, 5, and 6.8 m/s (left to right columns). Each row corresponds to measurements taken at $x_3 = 1.03$ and $x_3/h = 2.03$, respectively. Black $-5/3$ slope lines are placed at identical locations on all plots. Values of the horizontal length scale (red), Taylor length scale (blue), and Kolmogorov length scale (black) are given, and vertical dashed lines are plotted positioned at the frequencies associated with the length scales.

the turbulence structure accurately. These results confirm the adequacy of the probe dimensions, the quality of the measurements, and the effectiveness of the machine-learning-based calibration. Across all cases, the spectra reveal three characteristic regions: the energy-containing range, the ISR, and the dissipation range. As expected, increasing U_∞ results in a broader ISR and a shift toward higher frequencies (see Figs. 7, 8, 9, 10). The ISR is significantly narrower closer to the canopy than at higher elevations (see Fig. 7). At higher frequencies, spectral flattening is observed, occurring between 700 and 1300 Hz, depending on the vertical position and U_∞. This flattening indicates either reaching the noise floor or the smallest resolvable eddy scale of the flow. Black dashed vertical lines corresponding to the Kolmogorov scale frequency confirm that, in most cases, dissipation scales were indeed captured before encountering measurement noise, affirming the spectral fidelity. This ability to resolve Kolmogorov-scale frequencies is attributed to the combina-

tion of high-frequency CTA measurements, careful probe selection, and the machine-learning-based calibration workflow. Together, these ensure accurate quantification of turbulent fluctuations at the fine scales critical for canopy flow analysis.

Having established the fidelity of the spectral measurements in the homogeneous case, we next examine the TKE spectra at three representative positions in the heterogeneous configuration: positions 4, 7, and 12 (see Fig. 1). These span the spatial heterogeneity of the setup, with position 4 marking the onset of spanwise effects, position 7 located at the canopy edge, and position 12 deep inside the clear patch. Like in the homogeneous case, spectra are presented in Figs. 8 to 10 for the three free-stream velocities ($U_\infty = 3$, 5, and 6.8 m/s) and at two vertical locations ($x_3/h = 1.03$ and 2.03), with each column corresponding to a different U_∞. For comparison, corresponding homogeneous spectra based on u_1 (cyan) and u_2 (green) were added to each figure. A notable trend emerges in the heterogeneous layout. The ISR broadens progressively from position 4 to position 12, particularly at higher elevations. This progressive broadening is consistent with enhanced vertical mixing and the emergence of larger, energy-containing eddies downstream of the canopy edge, where the absence of obstruction allows turbulent structures to expand and reorganize freely (Pope 2001; Finnigan 2000). Additionally, the spectral shape flattening occurs at lower frequencies than in the homogeneous case, indicating earlier dissipation truncation of the turbulent cascade, likely a consequence of reduced high-wavenumber content and reduced turbulence intensity in the clear region.

Further spectral analysis reveals pronounced spatial variability in both spectral shape and energy content. At position 4 (Fig. 8), the spectral structure exhibits distinct elevation dependence. At the higher elevation ($x_3/h = 2.03$), spectra from heterogeneous and homogeneous layouts demonstrate excellent agreement, nearly collapsing onto each other across all velocities. This indicates limited sensitivity to canopy heterogeneity at twice the canopy height. However, at the canopy top ($x_3/h = 1.03$), clear differences are evident: spectral energy levels in the heterogeneous case are considerably higher for both u_1 and u_2, compared to their homogeneous counterparts. This discrepancy diminishes as the free-stream velocity increases, suggesting that higher momentum flows tend to mask the canopy-induced heterogeneity effects, likely due to enhanced mixing and turbulent transport across the shear layer.

At position 7 (canopy edge, Fig. 9), the spectra at both elevations ($x_3/h = 1.03$ and 2.03) do not exhibit collapse with the corresponding homogeneous cases, indicating pronounced local effects of canopy heterogeneity at the canopy edge. At this location, the proximity to the discontinuity between vegetated and clear regions creates enhanced local shear, intensified mixing, and the presence of intermittent, large-scale turbulent structures, which manifest as elevated low-frequency energy. Nevertheless, as the free-stream velocity increases, the spectral differences between homogeneous and heterogeneous cases diminish, suggesting that at higher velocities the turbulent structures become more
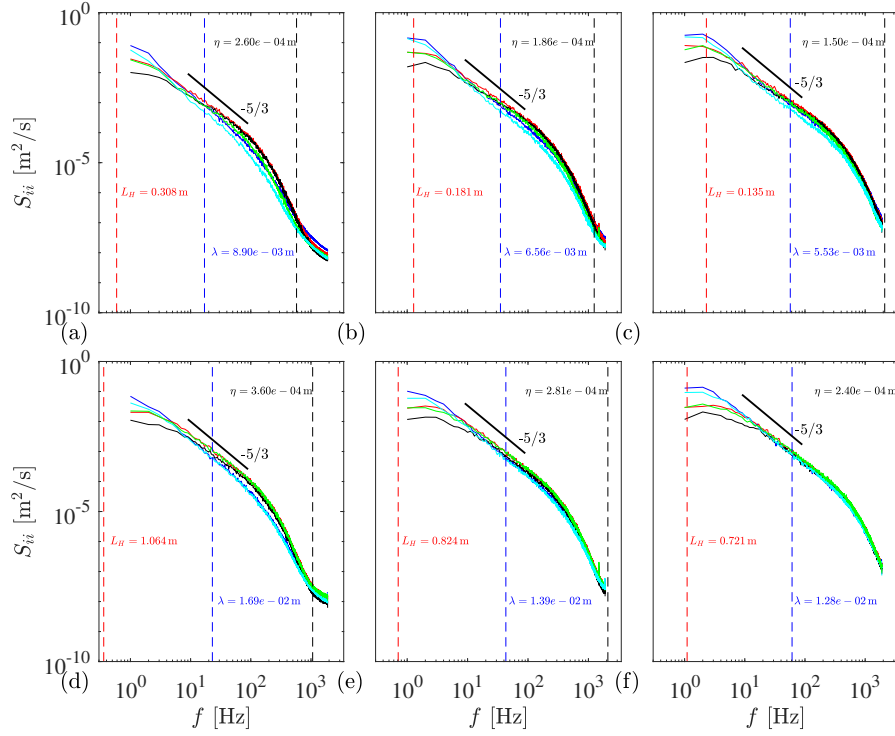
Fig. 8 Spectral analysis (position 4, heterogeneous layout): power density spectra of fluctuating velocity components u_1 (blue), u_2 (red), and u_3 (black), measured at $U_\infty = 3$, 5, and 6.8 m/s (left to right columns). Each row corresponds to measurements taken at $x_3 = 1.03$ and $x_3/h = 2.03$, respectively. For comparison, spectra from the homogeneous layout for u_1 (cyan) and u_2 (green) are overlaid. Black $-5/3$ slope lines are placed at identical locations on all plots. Values of the horizontal length scale (red), Taylor length scale (blue), and Kolmogorov length scale (black) are given, and vertical dashed lines are plotted at the frequencies associated with the length scales.

homogenized due to increased momentum transfer and reduced sensitivity to local canopy geometry.

At position 12 (clear patch, Fig. 10), the spectra show the most striking differences compared to the homogeneous configuration. Here, u_1 and u_2 spectra from heterogeneous and homogeneous layouts are markedly separated at both elevations and across all free-stream velocities, indicating sustained and substantial influence from upstream canopy heterogeneity. Specifically, the pronounced attenuation in the streamwise spectral density S_{11} reaches reductions up to an order of magnitude. This attenuation indicates a sharp decrease in turbulence intensity in regions lacking direct canopy forcing and underscores the role of vegetation drag and canopy-induced shear in sustaining TKE across scales. These observations correspond to the trends seen in turbulence dissipation rates and length scales that will be discussed in the following.
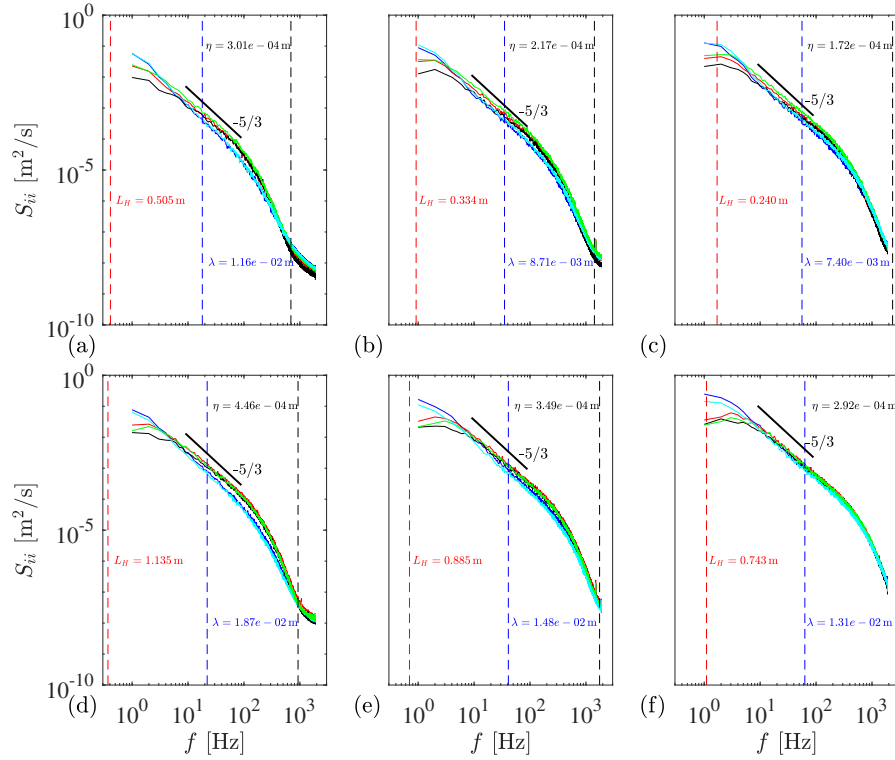
Fig. 9 Spectral analysis (position 7, heterogeneous layout): power density spectra of fluctuating velocity components u_1 (blue), u_2 (red), and u_3 (black), measured at $U_\infty = 3$, 5, and 6.8 m/s (left to right columns). Each row corresponds to measurements taken at $x_3 = 1.03$ and $x_3/h = 2.03$, respectively. For comparison, spectra from the homogeneous layout for u_1 (cyan) and u_2 (green) are overlaid. Black $-5/3$ slope lines are placed at identical locations on all plots. Values of the horizontal length scale (red), Taylor length scale (blue), and Kolmogorov length scale (black) are given, and vertical dashed lines are plotted at the frequencies associated with the length scales.

The observed spectral differences arise from the layout-induced modifications in TKE turbulence production and redistribution mechanisms. At the canopy edge (position 7), spanwise heterogeneity significantly enhances local shear and promotes the formation of large-scale intermittent structures, which contribute substantially to low-frequency energy and broaden the inertial subrange transition. In contrast, in the clear patch (position 12), the absence of canopy element drag combined with persistent upstream influences results in weaker production rates and less energetic eddies. Consequently, the turbulence spectra deviate markedly from classical rough-wall turbulence spectra, particularly evident in the distribution of energy across scales and the structure of the energy cascade.

Overall, spanwise heterogeneity primarily affects the energy-containing range of the turbulence (low frequencies) and the transition to the inertial range,

Fig. 10 Spectral analysis (position 12, heterogeneous layout): power density spectra of fluctuating velocity components u_1 (blue), u_2 (red), and u_3 (black), measured at $U_\infty = 3$, 5, and 6.8 m/s (left to right columns). Each row corresponds to measurements taken at $x_3 = 1.03$ and $x_3/h = 2.03$, respectively. For comparison, spectra from the homogeneous layout for u_1 (cyan) and u_2 (green) are overlaid. Black $-5/3$ slope lines are placed at identical locations on all plots. Values of the horizontal length scale (red), Taylor length scale (blue), and Kolmogorov length scale (black) are given, and vertical dashed lines are plotted at the frequencies associated with the length scales.

rather than eliminating the inertial cascade. At the canopy edge, a broad range of energetic turbulent eddies develops, spanning from large-scale mixing-layer structures down to smaller-scale wake-generated vortices. This broadened spectrum yields more complex spectral shapes compared to the homogeneous turbulence case, presenting significant implications for turbulence modeling within canopy flows. In contrast, turbulence spectra in regions distant from the canopy interface, either deep within vegetated areas or fully exposed clearings, tend to approach, but do not fully replicate, those of homogeneous canopy flows, reflecting persistent but subtle influences of spatial heterogeneity. These

findings emphasize that classical inertial-range scalings, such as Kolmogorov's $-5/3$ law, remain applicable locally, yet their precise onset, extent, and slope sensitivity are highly dependent on proximity to canopy heterogeneity.

3.3.2 Length scales

To obtain the characteristic length scales from single-point temporal data, we apply Taylor's frozen turbulence hypothesis, which enables the conversion of temporal scales into streamwise length scales. Although the validity of this assumption has been questioned in and near canopy flows (Kaimal and Finnigan 1994; Baldocchi and Meyers 1988), particularly due to non-stationarity and vertical advection, it remains a pragmatic tool for estimating characteristic scales in the outer flow. The fidelity of the present spectral measurements, together with consistent trends across positions and velocities, as discussed above, lends support to the use of Taylor's approximation in this context, especially above the canopy.
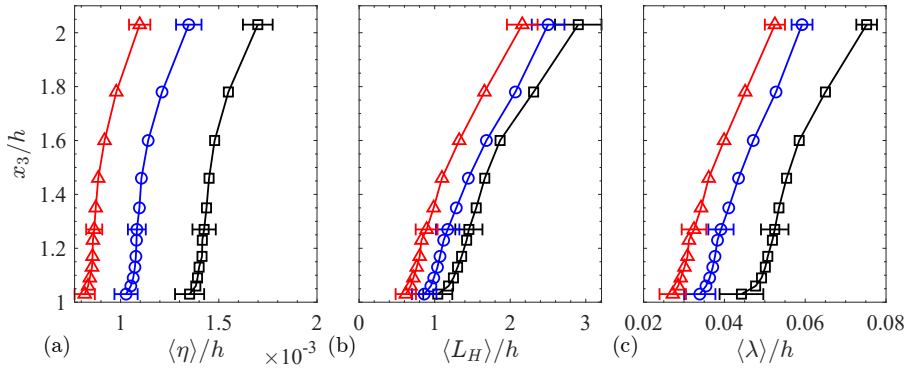
Fig. 11 Wall-normal profiles (homogeneous layout) of the normalized (a) Kolmogorov's length scale, (b) streamwise integral length scale, and (c) Taylor microscale, at $U_\infty = 3$ (black square), 5 m/s (blue circle), and 6.8 m/s (red triangle). Data points represent means across G2 (positions 4, 9, 11; within canopy) and G3 (positions 5, 8, 10, 12; between canopy). Error bars denote representative standard deviations.

The vertical distributions of the spatially averaged Kolmogorov (Eq. 2), Taylor (Eq. 9), and the streamwise integral (Eq. 10) length scales normalized by the canopy height are depicted in Fig. 11 for the homogeneous layout. Note that due to the small spanwise variability, the data were averaged over both G2 and G3 groups.

All three length scales increase with elevation, reflecting the larger energy-containing structures and reduced TKE dissipation rates. Their magnitudes, particularly the streamwise integral length scale, decrease systematically with increasing U_∞, consistent with increased turbulence intensity and smaller dominant structures at higher Reynolds numbers. At the canopy top ($x_3/h = 1.03$), the streamwise integral scale is approximately equal to the canopy height, but
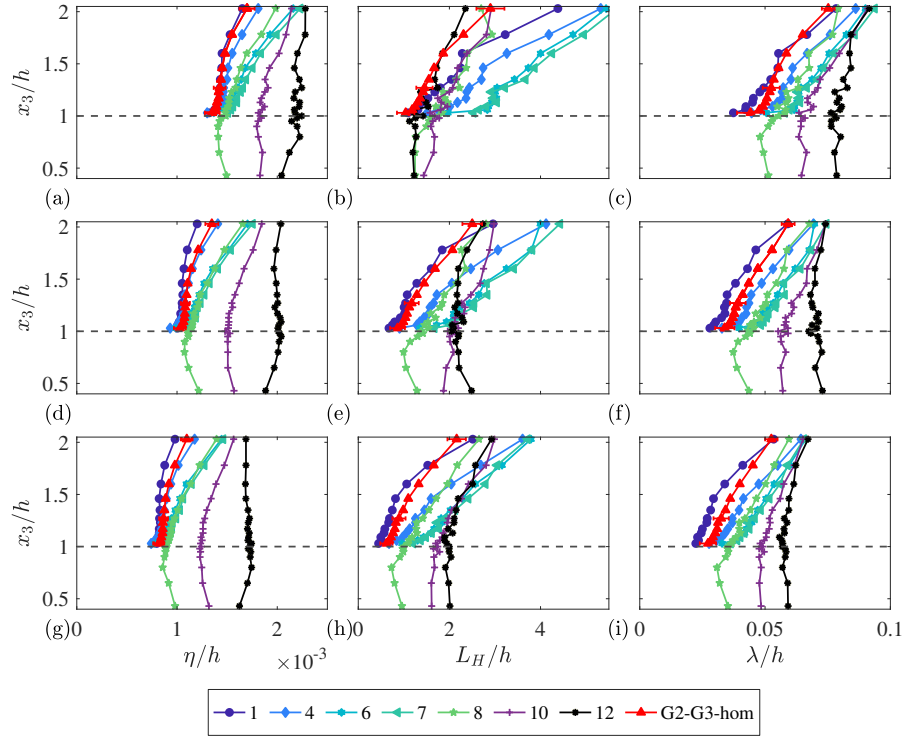
Fig. 12 Wall-normal profiles of η/h (first column), L_H/h (second column), and λ/h (third column) in heterogeneous layout. Measurement locations are 1, 4, 6, 7, 8, 10, and 12. Each row corresponds to measurements taken at $U_\infty = 3$, 5, and 6.8 m/s. For comparison, red lines show spatially averaged profiles in homogeneous layout, averaged over G2 (within canopy: 4, 9, 11) and G3 (between canopy: 5, 8, 10, 12); error bars denote representative standard deviations. Dashed horizontal lines indicate canopy height.

decreases by about 25% at the highest free-stream velocity. Further above, at $x_3/h = 2.03$, the integral scale exceeds twice the canopy height at all U_∞, coinciding with the spectral region where energy is injected into the flow, in line with the previous observations in homogeneous canopy flows (Kaimal and Finnigan 1994).

Figure 12 shows vertical profiles of η/h, L_H/h, and λ/h at selected positions in the heterogeneous layout (1, 4, 6, 7, 8, 10, and 12), alongside spatially averaged profiles from the homogeneous configuration (Fig. 11) for comparison. At $x_3/h = 1.03$, integral scales (middle column in Fig. 12) grow consistently toward the clear patch, reflecting increasing scales of energy-containing eddies in the absence of canopy obstruction. Conversely, at $x_3/h = 2.03$, the integral scale increases from within the canopy (position 4) to the canopy edge (position 7), but notably decreases by nearly 50% farther into the clear patch (position 12). This significant reduction highlights a distinct shift in turbulent dynamics above the clear region, where turbulence becomes less shear-driven
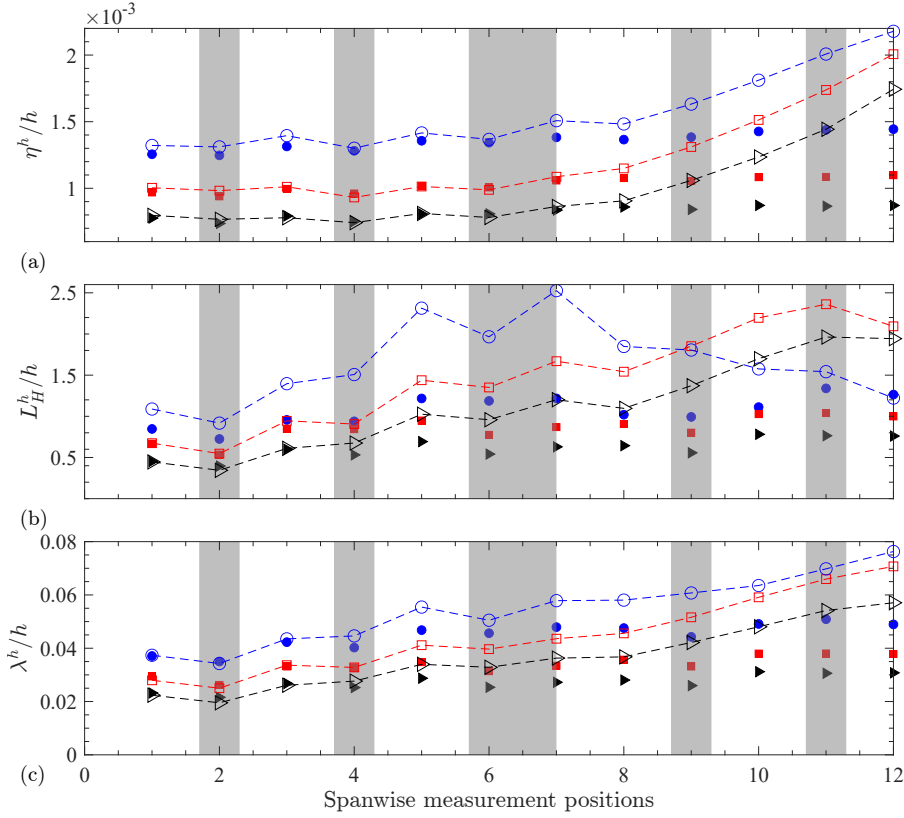
Fig. 13 Local normalized values of (a) Kolmogorov's length scale, (b) streamwise integral length scale, and (c) Taylor microscale at $x_3/h = 1.03$ (canopy height) at the 12 spanwise measurement positions. $U_\infty = 3$ m/s (blue circle), 5 m/s (red square), and 6.8 m/s (black triangle). Filled and open symbols correspond to the homogeneous and heterogeneous layouts, respectively. The gray shading indicates canopy obstructions.

and more characteristic of weakly perturbed boundary-layer conditions, indicative of reduced momentum exchange and weaker turbulent production aloft. Taylor length scales (right column in Fig. 12) exhibit in all cases a monotonic increase with increasing distance into the clear patch, consistent with an increasingly broad inertial subrange as previously indicated by the spectral analyses. Similarly, Kolmogorov length scales (left column in Fig. 12) increase in both vertical and spanwise directions, signaling progressively weaker viscous dissipation away from regions of strong canopy-induced turbulence. In agreement with the prior detailed spectral shapes analyses, these observations further support the observation that the spanwise canopy heterogeneity significantly changes the turbulent length scales compared to their homogeneous counterparts, primarily by modifying the balance between shear-driven TKE production and the TKE dissipation process. While the Kolmogorov length scales mainly deviate from their homogeneous counterparts within the clear

patch, the Taylor length scales and streamwise integral length scales show increased values inside the canopy extending across nearly all canopy heights of the spanwise edge. Again, confirming that the classical inertial-range scaling (Kolmogorov's -5/3 law) remains valid locally, with the transition scales, spectral slopes, and overall turbulence structure depend strongly on spatial proximity to the spanwise canopy heterogeneity. Complementing this, the spanwise variability at canopy height of η^h/h, λ^h/h, and L_H^h/h is shown in Fig. 13 at all measured positions. Kolmogorov scales, η^h/h, collapse for the homogeneous and heterogeneous layouts from position 1 through position 7, across all U_∞. This suggests that the smallest dissipative scales are not immediately affected by the canopy's spanwise heterogeneity and remain governed by local viscous dynamics. However, beyond the canopy edge (position 7), the two configurations begin to diverge, with the largest discrepancy observed at position 12 in the clear patch. The increased value of η^h/h in the heterogeneous case reflects weaker spatial velocity gradients and resulting reduced local dissipation. In contrast to η^h/h, the streamwise integral scale, L_H^h/h, diverges earlier from its homogeneous counterparts and increases from position 4 (within the canopy) to position 7 (canopy edge), peaking at position 12 in the clear patch. This spatial pattern is indicative of an increase in eddy sizes as the flow reorganizes downstream of the heterogeneous canopy interface, transitioning from smaller, canopy-generated wakes toward larger-scale coherent structures typical of smooth boundary-layer flows. Note that at the lowest $U_\infty(= 3 \text{ m/s})$, values of L_H^h/h diverge from the homogeneous layout values already at position 1, persisting through position 8, with the largest disparity near the canopy edge (position 7). Interestingly, in this low-momentum case, the integral scale returns to its homogeneous layout value at position 12, reflecting the flow's eventual reorganization in the absence of canopy forcing. The normalized Taylor microscales, λ^h/h, also collapse between the homogeneous and heterogeneous layouts up to position 4, regardless of U_∞. Beyond this position, λ^h/h grows progressively in the heterogeneous case, especially as the flow transitions past the canopy edge. This increase reflects the emergence of larger intermediate scales and agrees with the reduced production and elevated coherence of turbulent structures observed in the spectral analysis.

3.3.3 Turbulence intensity, TKE and TKE dissipation rates

Next, a detailed examination of the vertical and spanwise distributions of TI, TKE, and the TKE dissipation rate, with emphasis on deviations from canonical boundary layer behavior due to canopy-induced heterogeneity, is presented. Figure 14 presents wall-normal profiles of these quantities for the homogeneous layout, averaged over groups G2 and G3, across all U_∞. As expected for canopy flows, upon approaching the canopy from the top, the turbulence intensity increases, peaking at $x_3/h \approx 1$, consistent across all U_∞, with slightly higher TI values observed at greater U_∞. In contrast, the TKE profiles (Fig.14b) show a peak at $x_3/h \approx 1.5$, before decreasing sharply near the canopy top. This TKE peak above the canopy height agrees with prior

graphics/Figure14.pdf
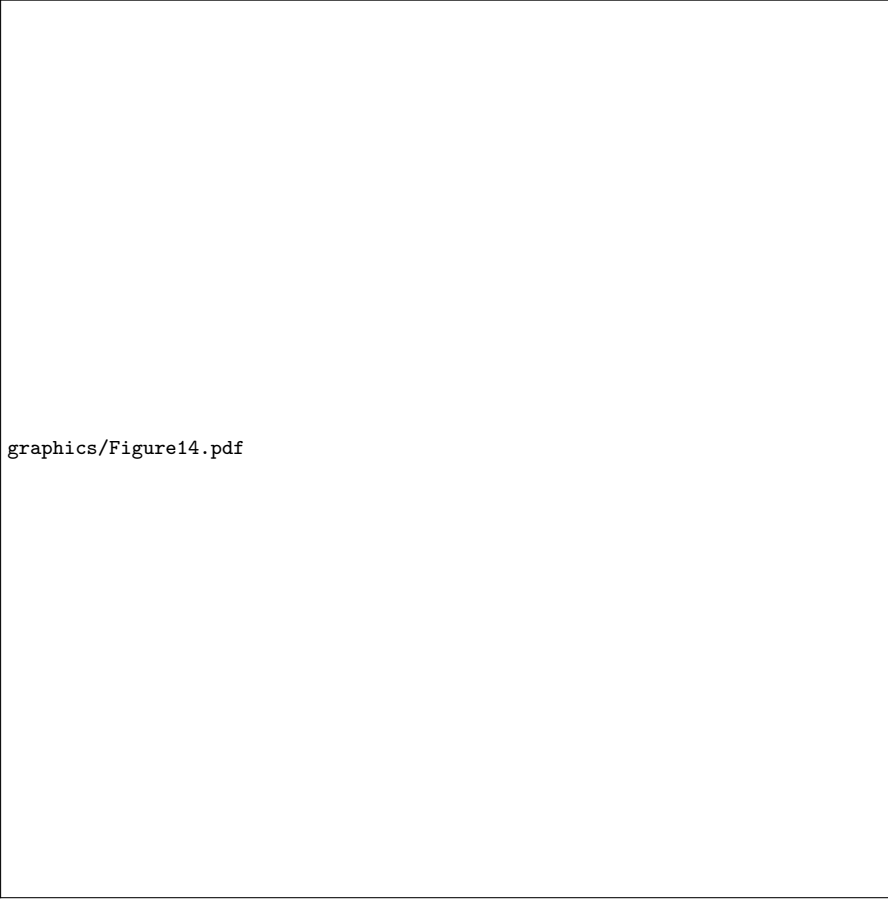
Fig. 14 Wall-normal profiles of (a) $\langle TI \rangle$, (b) $\langle TKE \rangle / U_\infty^2$, and (c) $\langle \bar{\epsilon} \rangle / \frac{(\mathrm{TKE})^{3/2}}{h}$ at $U_\infty = 3$ (black square), 5 (blue circle), and 6.8 m/s (red triangle) for the homogeneous layout. Curves represent means across G2 (positions 4, 9, 11; within canopy) and G3 (positions 5, 8, 10, 12; between canopy). Error bars denote standard deviation.

findings on enhanced turbulence due to inflection-point shear layers at the canopy-air interface. Normalized dissipation profiles (Fig.14c) follow a classical pattern for rough-wall turbulent boundary layers with vegetation: minimal dissipation aloft, increasing steeply with proximity to the canopy, and peaking sharply at $x_3/h = 1$. This behavior is indicative of the rapid energy transfer to small scales facilitated by vegetation-induced shear and wake production (Ayotte et al. 1999; Finnigan 2000), reinforcing the physical linkage between inflectional instabilities and efficient TKE dissipation. Figure 15 displays the spanwise variation of the normalized TKE and $\bar{\epsilon}$ at canopy height across all 12 positions. For TKE (Fig. 15a), values in the heterogeneous layout diverge from those in the homogeneous case at position 4. Initially, TKE increases relative to the homogeneous reference case, with the largest differences between
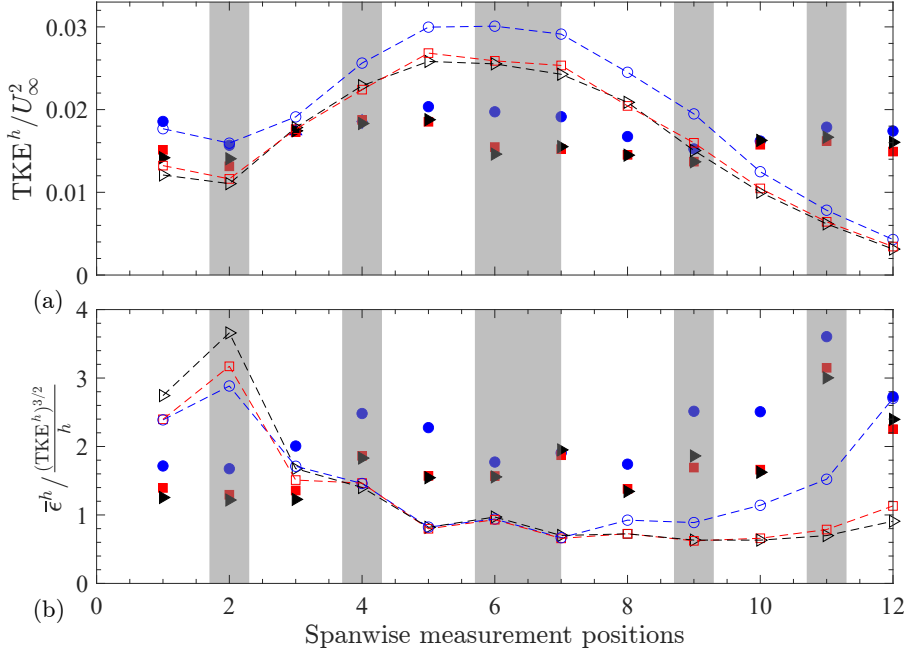
Fig. 15 Local values at $x_3/h = 1.03$ (canopy height) of (a) $\mathrm{TKE}^h/U_\infty^2$, and (b) $\bar{\epsilon}^h / \frac{(\mathrm{TKE}^h)^{3/2}}{h}$ at the 12 spanwise measurement positions for $U_\infty = 3$ m/s (blue symbols), 5 m/s (red symbols), and 6.8 m/s (black symbols). Filled and open symbols correspond to the homogeneous and heterogeneous layouts, respectively. The gray shading indicates canopy obstructions.

positions 6 and 8, straddling the canopy edge (position 7), where spatial heterogeneity appears to strongly enhance local turbulence production through increased shear and spatial intermittency. Going into the clear patch, starting at positions 6, 7, values of $\mathrm{TKE}^h/U_\infty^2$ decrease and fall below those of the homogeneous layout as turbulence in the clear patch weakens due to reduced production and the absence of canopy drag. Note that at the two highest free-stream velocities ($U_\infty = 5$ and 6.8 m/s), values of $\mathrm{TKE}^h/U_\infty^2$ nearly collapse at all spanwise positions. Spanwise profiles of normalized values of $\bar{\epsilon}^h$ (Fig. 15b) are strikingly different from those of TKE^h (Fig. 15a). Values of $\bar{\epsilon}^h h/(\mathrm{TKE}^h)^{3/2}$ for the heterogeneous layout significantly exceed those of the homogeneous reference case at positions 1 and 2. This is followed by a sharp drop at position 3, indicating rapid dissipation decay over short spanwise distances. From positions 4 through 12, $\bar{\epsilon}^h h/(\mathrm{TKE}^h)^{3/2}$ in the heterogeneous layout remain consistently lower than in the homogeneous case, despite the elevated TKE levels observed across the canopy edge. The largest discrepancy occurs at position 12, deep within the clear patch, where dissipation in the heterogeneous case remains low, reflecting reduced small-scale activity and diminished turbulent strain, while the homogeneous case retains elevated values due to ongoing canopy-generated turbulence. This decoupling between energy
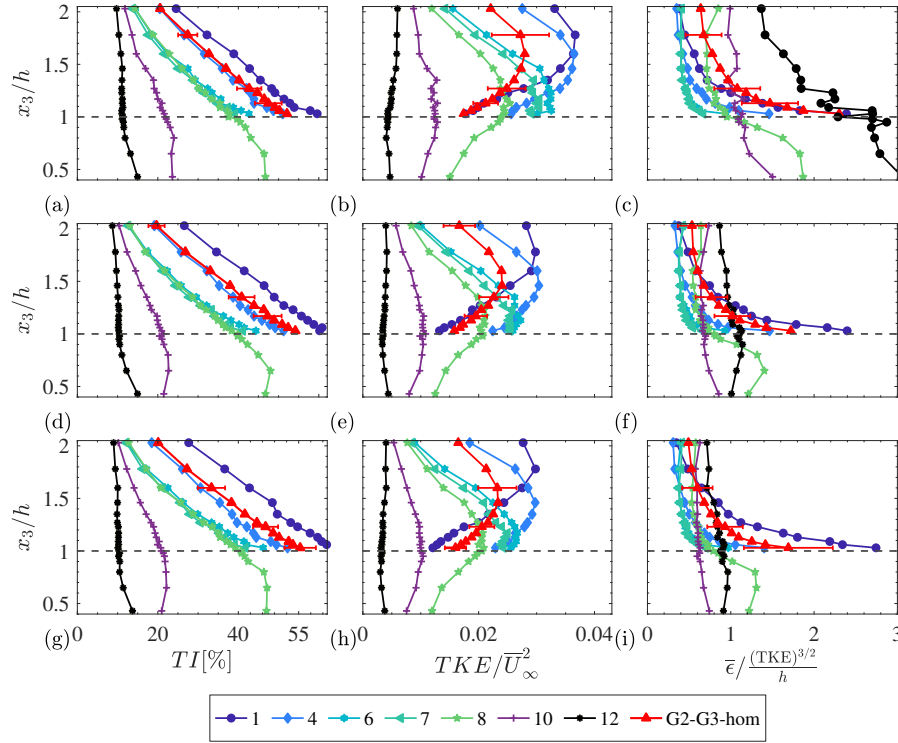
Fig. 16 Wall-normal profiles of TI [%] (1st column), $TKE/\overline{U}_\infty^2$ (2nd column), and $\overline{\epsilon}/\frac{(\text{TKE})^{3/2}}{h}$ (3rd column) in the heterogeneous layout at positions 1, 4, 6, 7, 8, 10, and 12. Rows correspond to $U_\infty = 3$, 5, and 6.8 m/s. For comparison, red lines show spatially averaged profiles in the homogeneous layout, averaged over G2 (within canopy: 4, 9, 11) and G3 (between canopy: 5, 8, 10, 12); error bars denote representative standard deviations. Dashed horizontal lines indicate canopy height.

content and dissipation in the heterogeneous layout suggests a shift in the turbulent cascade dynamics across the canopy edge, driven by the absence of direct forcing and a widening inertial range.

The wall-normal profiles of TI, normalized TKE, and $\overline{\epsilon}$ for the heterogeneous case shown in Fig. 16, further highlight how spanwise variations modify turbulence statistics. Wall-normal profiles are provided at positions 1, 4, and 6 (above canopy), 7 (edge), and 8, 10, and 12 (open patch). For comparison, red lines show spatially averaged profiles from the homogeneous layout, computed over positions in G2 (within canopy: 4, 9, 11) and G3 (between canopy: 5, 8, 10, 12).Turbulence intensity (left column in Fig. 16) remains the highest directly above the canopy elements and decays steadily into the open patch. At position 12, TI becomes nearly constant from $x_3/h = 2.03$ to $x_3/h = 0.7$, indicating a vertically uniform layer with weak turbulent production and limited vertical mixing, likely due to the absence of canopy-induced shear. Comparisons with the homogeneous reference reveal strong agreement at position 4,

but noticeable TI reductions at positions 6 and 7, underscoring the impact of the spanwise heterogeneity on the near-edge turbulence.

The TKE profiles (middle column in Fig. 16) reveal key differences between the heterogeneous and homogeneous configurations. While the homogeneous case exhibits a distinct TKE peak near $x_3/h \approx 1.5$, commonly attributed to inflectional shear-layer instabilities above the canopy, this peak is shifted in the heterogeneous layout from $x_3/h \approx 1.8$ at position 1 to $x_3/h \approx 1.1$ at position 8. This difference likely reflects the disrupted vertical coherence of shear layers caused by spanwise heterogeneity, which modifies the structure and intensity of inflectional instabilities. Furthermore, at positions 1 and 4, TKE magnitudes in the heterogeneous case are substantially higher near the canopy top. In the open patch, TKE exhibits a more gradual vertical structure. The localized peak at position 8 ($x_3/h \approx 1.1$) weakens further and disappears at position 12, where a near-uniform vertical profile is obtained. This progressive damping suggests a lack of strong production mechanisms in the clear region, in line with earlier observations of spectral energy depletion and reduced inertial-range scaling.

The normalized TKE dissipation rate profiles (Fig. 16, right column) further emphasize the effects of heterogeneity. At positions 4 and 6, the dissipation rate profiles are nearly identical in shape to those of the homogeneous case. However, at positions 6 and 7, values of $\bar{\epsilon}h/(\mathrm{TKE})^{3/2}$ are markedly lower than the homogeneous baseline case. In the clear patch, profiles flatten with elevation, indicating minimal vertical energy transport. Note that at the lowest flow velocity, position 12 exhibits a strong dissipation peak near the ground, possibly linked to secondary shear layers forming due to residual turbulence decay or floor roughness effects.

Altogether, these results demonstrate that spanwise heterogeneity primarily affects TKE generation and dissipation near canopy edges and into the clear patch, where both production mechanisms and spectral energy cascades are altered. The comparison between homogeneous and heterogeneous layouts reveals that while turbulent production mechanisms remain robust above the canopy, their spatial imprint upon approaching the canopy is highly sensitive to local geometry. Persistent dissipation downstream of the canopy edge, despite reduced TKE, underscores the role of advective coherent structures and lingering shear zones in sustaining turbulent energy transfer even in seemingly "quiescent" regions. These findings support and extend the spectral and length-scale observations discussed previously, providing a coherent picture of how spatial heterogeneity modulates not only turbulence intensity and structure but also the full cascade from production to dissipation.

3.3.4 Inertial range scaling

To further assess the turbulence cascade, we plot the compensated TKE spectra and evaluate deviations from classical inertial-range scaling, focusing on spectral plateau behavior and semi-empirical Kolmogorov constants. In canonical turbulence, a well-developed inertial range is characterized by a flat com-
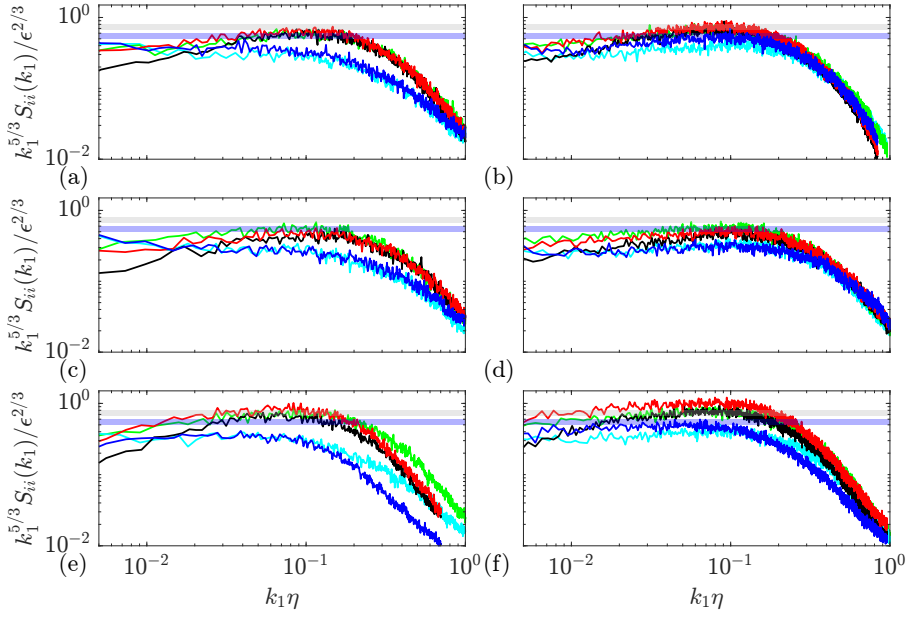
Fig. 17 Compensated spectra $k_1^{5/3} S_{ii}(k_1)/\epsilon^{2/3}$ at $x_3/h = 1.03$ for $U_\infty = 3$ m/s (left column) and 6.8 m/s (right column), and positions 4, 7, and 12 (rows from top to bottom). Spectra are shown for u_1 (blue), u_2 (red), and u_3 (black) of the heterogeneous layout. For comparison, spectra from the homogeneous layout are overlaid for u_1 (cyan) and u_2 (green). Horizontal shaded bands indicate the canonical Kolmogorov constant ranges: blue for $C_1^{(11)} \approx 0.5$–0.6, and gray for $C_1^{(22)}$, $C_1^{(33)} \approx 0.67$–0.8.

788 pensated spectrum over a range of intermediate wavenumbers. This plateau re-
789 flects a scale-invariant energy cascade governed by local interactions, with the
790 plateau level corresponding to the semi-empirical Kolmogorov constants, $C_1^{(ii)}$.
791 Deviations from this ideal behavior, such as tilting, curvature, or amplitude
792 suppression, typically indicate distortions to the cascade due to anisotropy,
793 inhomogeneity, or insufficient scale separation. With the help of the follow-
794 ing results, we evaluate if and where classical isotropic assumptions hold and
795 where canopy-induced heterogeneity reshapes spectral energy transfer.

796 Example compensated spectra, $k_1^{5/3} S_{ii}(k_1)/\epsilon^{2/3}$, at three spanwise posi-
797 tions (4, 7, and 12) in the heterogeneous canopy layout plotted against the
798 normalized wavenumber $k_1\eta$, are depicted in Figs. 17 and 18 at $x_3/h = 1.03$
799 and 2.03, respectively. These positions correspond to locations above a canopy
800 element, at the canopy edge, and within the open patch, respectively. Spectra
801 are shown for two free stream velocities ($U_\infty = 3$ and 6.8 m/s). The three
802 velocity components are plotted in blue (u_1), red (u_2), and black (u_3), with
803 shaded bands added to guide interpretation: a blue band marks the canonical
804 streamwise range $C_1^{(11)} \approx 0.5$-0.6, and a gray band highlights the transverse
805 range $C_1^{(22)}$, $C_1^{(33)} \approx 0.67$-0.8 (Pope 2001). For reference, corresponding spec-
806 tra for the homogeneous layout are included in cyan (u_1) and green (u_2) to
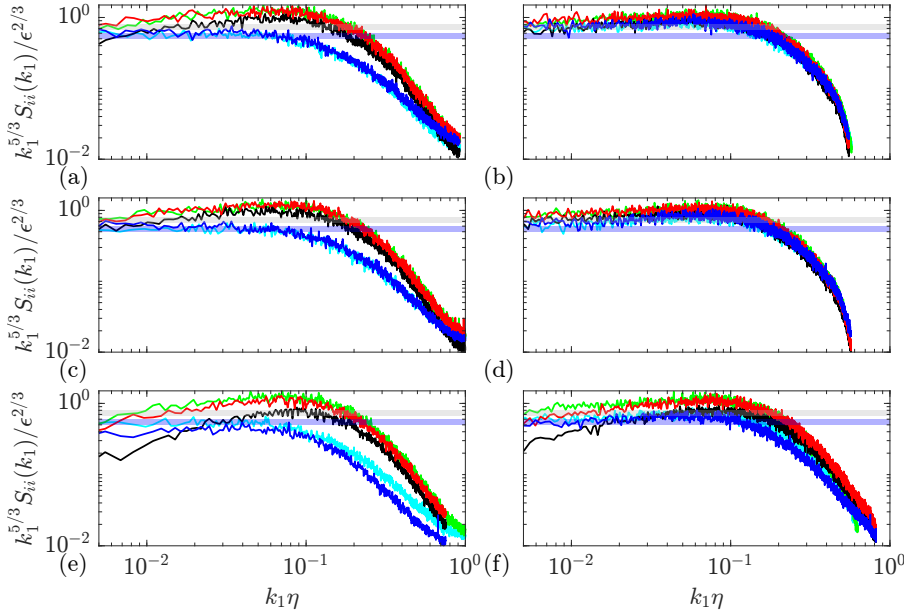
Fig. 18 Compensated spectra $k_1^{5/3} S_{ii}(k_1)/\epsilon^{2/3}$ at $x_3/h = 2.03$ for $U_\infty = 3$ m/s (left column) and 6.8 m/s (right column), and positions 4, 7, and 12 (rows from top to bottom). Spectra are shown for u_1 (blue), u_2 (red), and u_3 (black) of the heterogeneous layout. For comparison, spectra from the homogeneous layout are overlaid for u_1 (cyan) and u_2 (green). Horizontal shaded bands indicate the canonical Kolmogorov constant ranges: blue for $C_1^{(11)} \approx 0.5$–0.6, and gray for $C_1^{(22)}$, $C_1^{(33)} \approx 0.67$–0.8.

facilitate direct comparison between layouts. Note that spectra based on u_3 closely resemble those of u_2 (see Fig. 7) and are not depicted here.

In general, in most cases, there is a discrepancy between the canonical smooth wall values of $C_1^{(ii)}$ and those obtained for the homogeneous and heterogeneous layouts. At twice the canopy height (Fig. 18), "plateaus" become more pronounced, especially at the highest U_∞ (right column in Fig. 18). Not surprisingly, this indicates that the anisotropy effects as a result of the underlying canopy are reduced with increasing height. At the lowest freestream velocity (left columns in Figs. 17 and 18), none of the spectra exhibit a clear inertial-range plateau. This improves at $x_3/h = 2.03$ (left column in Fig. 18), but still significant discrepancies exist between canonical values and the measured plateau values. At the highest freestream velocity (right columns in Figs. 17 and 18), compensated spectra at positions 4 and 12 display reasonably flat plateaus for u_1, with values close to the canonical ones. This indicates that stronger mean shear and turbulence intensity support a more developed cascade, even in the presence of heterogeneity. Nevertheless, position 7 continues to show disrupted scaling, confirming that the canopy edge remains a zone of elevated anisotropy and turbulence distortion, regardless of flow strength. Comparison with the homogeneous layout across all panels shows that while

higher velocities promote convergence between layouts at positions 4 and 12 in the heterogeneous layout, the canopy edge (position 7) persistently disrupts inertial-range organization.

Comparing the compensated spectra for u_1 and u_2 for the homogeneous and heterogeneous layouts shows that at positions 4 and 7, they closely align both in shape and in magnitude, suggesting that turbulence above a canopy element remains relatively unaltered by the spanwise heterogeneity even at the canopy edge.

At position 12 (bottom rows in Figs. 17 and 18), deep in the open patch, the heterogeneous spectra clearly deviate from the homogeneous ones, showing reduced energy levels at high wavenumbers ($\kappa_1 \eta > 0.1$, especially for $S_{11}(k_1)$ as a result of the absence of canopy forcing. In addition, "plateaus" are less pronounced.

At the highest streamwise velocity ($U_\infty = 6.8$ m/s), the inertial-range plateaus are not only well-defined but are elevated above the canonical constant values at positions 4 and 7 (Figs. 18b, d) This consistent shift across all velocity components suggests enhanced energy content at intermediate scales, likely driven by vertical transport of energetic structures originating from the canopy. The elevated plateau levels above the canopy elements point to ejection-driven dynamics and possible nonlocal energy transfer, particularly at the canopy edge and above individual canopy elements. Notably, the similarity between positions 4 and 7 at this height (Fig.18b, d) indicates a convergence in spectral shape and energy distribution, despite differing near-canopy turbulence regimes. In contrast, position 12 (Fig. 18f) adheres more closely to canonical values, reflecting weaker vertical coupling and reduced turbulent energy injection from below. Overall, the strong collapse between homogeneous and heterogeneous spectra at $x_3/h = 2.03$, especially at the highest velocity, demonstrates that canopy-induced heterogeneity primarily distorts turbulence locally near the canopy top. Farther aloft, the turbulent structure recovers classical inertial-range behavior, largely independent of the underlying spatial variability.

Vertical profiles of the measured values of $C_1^{(11)}$, $C_1^{(22)}$, and $C_1^{(33)}$ (see section 2.3), for both the homogeneous (filled markers) and heterogeneous (open markers) layouts are shown in Fig. 19 in blue, red, and black, respectively. Rows correspond to the three spanwise positions (4, 7, and 12), while columns distinguish between the two free-stream velocities ($U_\infty = 3$ and 6.8 m/s). These profiles provide a quantitative basis for assessing how canopy heterogeneity modulates inertial-range behavior and local isotropy with increasing elevation. These results confirm and extend the trends observed in the example compensated spectra plotted in Figs. 17 to 18. The values of $C_1^{(ii)}$ for the homogeneous layout strongly deviate from the canonical values at all positions and for most heights. The correspondence seen at some heights (e.g. $C_1^{(22)}$ and $C_1^{(33)}$ for $1.2 < x_3/h < 1.5$ in Fig. 19d) appears to be coincidental. At positions 4 and 7, and across most heights and velocity components, values of $C_1^{(ii)}$ are similar for the homogeneous and heterogeneous layouts, with particularly
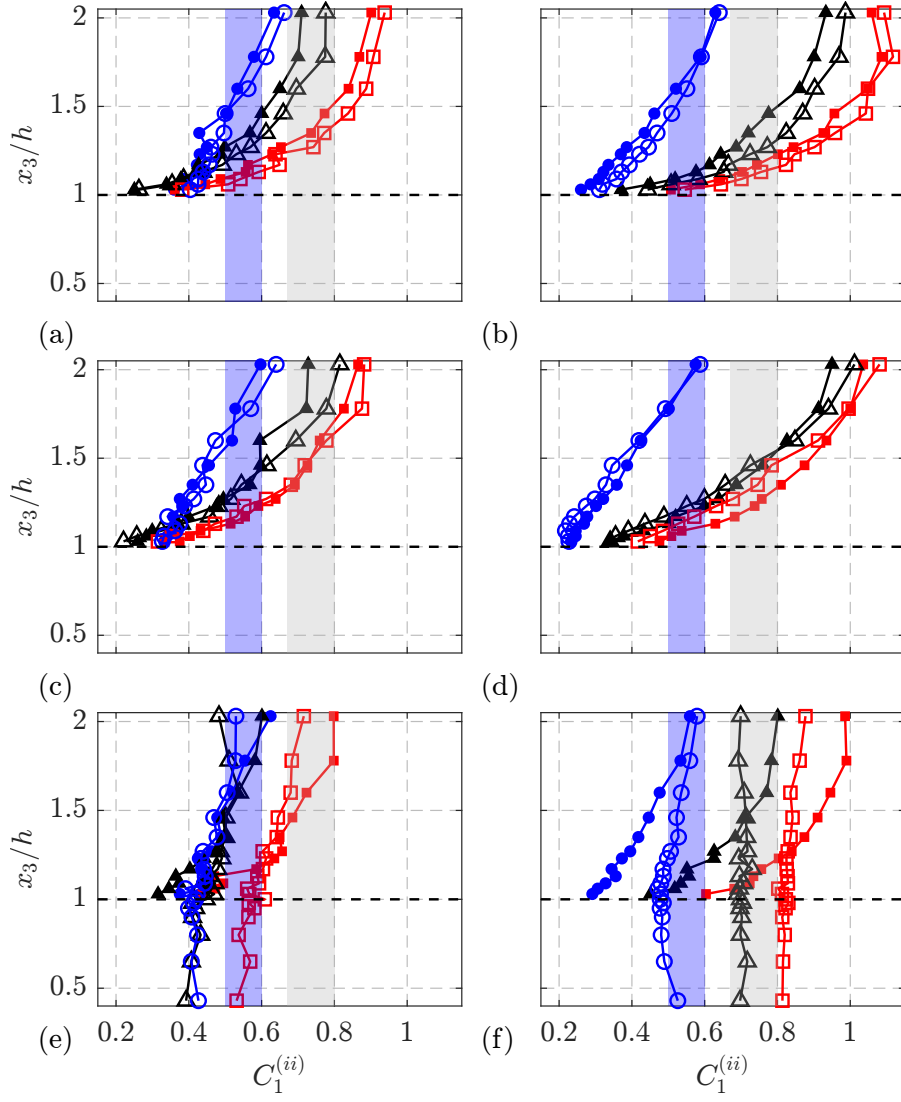
Fig. 19 Vertical profiles of empirical Kolmogorov constants $C_1^{(11)}$ (blue), $C_1^{(22)}$ (red), and $C_1^{(33)}$ (black) at positions 4, 7, and 12 (rows from top to bottom), for $U_\infty = 3$ m/s (left column) and 6.8 m/s (right column). Filled markers correspond to the homogeneous layout, and open markers denote the heterogeneous layout. Vertical shaded bands indicate canonical ranges: blue for $C_1^{(11)} \approx 0.5\text{-}0.6$, and gray for $C_1^{(22)}$, $C_1^{(33)} \approx 0.67\text{-}0.8$. Dashed horizontal lines indicate the canopy height.

good agreement for $C_1^{(11)}$, indicating that streamwise cascade behavior is less sensitive to spanwise heterogeneity than the transverse components. Only at position 12, homogeneous and heterogeneous layout results are different. The heterogeneous layout results for $C_1^{(ii)}$ as a function of height indicate near vertical profiles with reasonable collapse with the canonical values of $C_1^{(ii)}$, especially for the highest U_∞ (Fig. 19f). However, note that $C_1^{(22)} > C_1^{(33)}$, indicating that proximity to the spanwise heterogeneity still induces a considerable anisotropy even at position 12 in the clear patch.

4 Summary and conclusions

This study has presented a detailed investigation of turbulent flow structure across a spanwise-heterogeneous vegetative canopy model using high-resolution constant-temperature anemometry. By integrating this technique with a novel machine learning-based calibration approach, we achieved accurate, high-frequency measurements of both mean and fluctuating velocity components spanning a broad range of scales. Crucially, this approach enabled a full resolution of the TKE spectra down to the smallest dissipative scales. A rigorously controlled experimental framework facilitated the collection of a comprehensive dataset, capturing spatially complex flow dynamics across both spanwise and wall-normal directions.

Measurements were performed over a homogeneous as well as a heterogeneous canopy layout. The homogeneous layout results served as a baseline, confirming a stable turbulence structure with minimal spanwise variability above the canopy. In contrast, the heterogeneous layout revealed substantial spatial variability in both mean and turbulent flow properties. Over the open patch, the boundary layer resembled classical rough-wall turbulence, developing in a manner distinct from the vegetated patch. Across all tested freestream velocities, systematic reductions in TKE and dissipation were observed above and near the canopy, indicating robust modifications induced by spatial heterogeneity.

The use of CTA facilitated the collection of high-frequency, multi-point turbulence statistics through extended measurement durations and carefully chosen sensor dimensions. These measurements yielded robust insights into the impact of spanwise heterogeneity on both the mean flow and turbulence properties. The results revealed strong modulation of spectral energy and dissipation, providing clear evidence that spanwise canopy heterogeneities significantly affect the turbulence cascade and spatial organization of energy within and above vegetative canopies.

The spectral analysis revealed systematic deviations from canonical inertial-range behavior linked directly to spanwise canopy heterogeneity. In regions far from the canopy edge, either over the open patch or above the canopy, compensated spectra exhibited well-defined inertial subranges consistent with the classical $-5/3$ scaling and Kolmogorov constants $C_1^{(11)} \approx 0.5$, in agreement with surface-layer theory. However, near the canopy edge (position 7),

all components exhibited distorted spectra with elevated or flattened plateaus, especially in the transverse directions. These distortions point to an altered cascade, likely driven by local anisotropy and shear-layer production at the vegetation interface.

The corresponding empirical Kolmogorov constants, $C_1^{(ii)}$, showed clear spatial trends: at low flow rates, values across all positions deviated from the canonical plateau range, but at higher flow rates, positions 4 and 12 exhibited strong recovery toward classical constants, while at the spanwise edge position, values continued to deviate. Vertical profiles of $C_1^{(ii)}$ further confirmed that while local isotropy is recovered aloft (at $x_3/h = 2.03$) in many regions, the canopy edge continues to act as a spectral disturbance source, altering the directional energy transfer and reducing the efficiency of inertial-range development.

These results provide direct experimental evidence that spanwise canopy heterogeneity introduces spectral distortions not only near the vegetation but also aloft through the ejection of energetic structures. The breakdown of universality in the inertial-range plateau near the edge reinforces the growing understanding that inhomogeneous boundary conditions can imprint persistent structural signatures across scales.

Profiles of mean velocity, TKE, and length scales exhibited pronounced variation across spanwise positions. At the canopy edge (position 7), enhanced turbulence intensity and elevated TKE were observed, signaling strong local shear interactions between the vegetation and overlying flow. Deeper into the clear patch (position 12), TKE declined sharply, accompanied by significant shifts in both the Taylor length scale and the horizontal integral length scales. These shifts highlight structural transitions in turbulence, driven by edge-induced shear and its downstream influence on coherent eddies and energy transfer. The observed spatial variations in spectral shape, dissipation rates, and empirical $C_1^{(ii)}$ values collectively challenge the assumption of universal inertial-range scaling in canopy flows. In particular, the canopy edge emerges as a localized disruption zone where the energy cascade is modified, anisotropy persists, and classical scaling laws break down. These findings not only validate emerging theories of inhomogeneity-modified turbulence but also emphasize the need to revise isotropy-based assumptions in turbulence closures.

In summary, this study provides comprehensive experimental evidence that spanwise heterogeneity substantially alters turbulence spectra, dissipation, and momentum transport mechanisms in canopy flows. These results have direct implications for turbulence closure models in atmospheric and environmental simulations. Incorporating these empirical findings into numerical frameworks will enhance predictive fidelity in applications involving wind transport, pollutant dispersion, and land–atmosphere exchange. The presented data and analysis establish a rare, high-resolution benchmark for validating large-eddy simulations and turbulence theories in heterogeneous environments. Ultimately, the results contribute to a refined understanding of turbulent cascades in complex,

fragmented surface layers, offering a valuable reference point for advancing both empirical and theoretical models of canopy-layer turbulence.

Electronic Supplementary Material Supplementary material includes additional figures. These are available in the online version of the article at SpringerLink.

References

Amiro B (1990) Drag coefficients and turbulence spectra within three boreal forest canopies. Boundary-Layer Meteorology 52:227–246

Anderson W, Barros JM, Christensen KT, Awasthi A (2015) Numerical and experimental study of mechanisms responsible for turbulent secondary flows in boundary layer flows over spanwise heterogeneous roughness. Journal of Fluid Mechanics 768:316–347, DOI 10.1017/jfm.2015.91

Antonia RA, Luxton RE (1972) The response of a turbulent boundary layer to a step change in surface roughness. Part 2. Rough-to-smooth. Journal of Fluid Mechanics 53(4):737–757, DOI 10.1017/S002211207200045X

Vilà-Guerau de Arellano J, Hartogensis O, Benedict I, De Boer H, Bosman PJ, Botía S, Cecchini MA, Faassen KA, González-Armas R, Van Diepen K, et al. (2023) Advancing understanding of land–atmosphere interactions by breaking discipline and scale barriers. Annals of the New York Academy of Sciences 1522(1):74–97

Ayotte KW, Finnigan JJ, Raupach MR (1999) A second-order closure for neutrally stratified vegetative canopy flows. Boundary-Layer Meteorology 90(2):189–216

Baldocchi DD, Meyers TP (1988) A spectral and lag-correlation analysis of turbulence in a deciduous forest canopy. Boundary-Layer Meteorology 45:31–58

Banerjee T, Brugger P, De Roo F, Kröniger K, Yakir D, Rotenberg E, Mauder M (2018) Turbulent transport of energy across a forest and a semiarid shrubland. Atmospheric Chemistry and Physics 18(13):10,025–10,038

Belcher S, Jerram N, Hunt J (2003) Adjustment of a turbulent boundary layer to a canopy of roughness elements. Journal of Fluid Mechanics 488:369–398

Bonan GB, Patton EG, Harman IN, Oleson KW, Finnigan JJ, Lu Y, Burakowski EA (2018) Modeling canopy-induced turbulence in the Earth system: A unified parameterization of turbulent exchange within plant canopies and the roughness sublayer (CLM-ml v0). Geoscientific Model Development 11(4):1467–1496

Bou-Zeid E, Meneveau C, Parlange MB (2004) Large-eddy simulation of neutral atmospheric boundary layer flow over heterogeneous surfaces: Blending height and effective surface roughness. Water Resources Research 40(2)

Bou-Zeid E, Parlange MB, Meneveau C (2007) On the parameterization of surface roughness at regional scales. Journal of the atmospheric sciences 64(1):216–227

Bou-Zeid E, Anderson W, Katul GG, Mahrt L (2020) The persistent challenge of surface heterogeneity in boundary-layer meteorology: a review. Boundary-Layer Meteorology 177:227–245

Brugger P, Banerjee T, De Roo F, Kröniger K, Qubaja R, Rohatyn S, Rotenberg E, Tatarinov F, Yakir D, Yang F, et al. (2018) Effect of surface heterogeneity on the boundary-layer height: a case study at a semi-arid forest. Boundary-Layer Meteorology 169:233–250

Brunet Y (2020) Turbulent flow in plant canopies: historical perspective and overview. Boundary-Layer Meteorology 177(2-3):315–364

Brunet Y, Collineau S, Shaw RH, Maitani T, Qiu J, Hipps L, et al. (1992) On coherent structures in turbulence above and within agricultural plant canopies. Agricultural and forest meteorology 61(1-2):55–68

Brunet Y, Finnigan J, Raupach M (1994) A wind tunnel study of air flow in waving wheat: single-point velocity statistics. Boundary-Layer Meteorology 70(1):95–132

Brutsaert W (1998) Land-surface water vapor and sensible heat flux: Spatial variability, homogeneity, and measurement scales. Water Resources Research 34(10):2433–2442

Bruun HH (1996) Hot-wire anemometry: principles and signal analysis. Measurement Science and Technology 7(10):024

Cheng H, Castro IP (2002) Near-wall flow development after a step change in surface roughness. Boundary-Layer Meteorology 105:411–432

Chung D, Monty JP, Hutchins N (2018) Similarity and structure of wall turbulence with lateral wall shear stress variations. Journal of Fluid Mechanics 847:591–613

van Dijk A, Nieuwstadt F (2004) The calibration of (multi-) hot-wire probes. 2. Velocity-calibration. Experiments in fluids 36:550–564

Dupont S, Brunet Y (2009) Coherent structures in canopy edge flow: A large-eddy simulation study. Journal of Fluid Mechanics 630:93–128, DOI 10.1017/S0022112009006739

Finnigan J, Shaw RH, Patton EG (2009) Turbulence structure above a vegetation canopy. Journal of Fluid Mechanics 637:387–424, DOI 10.1017/S0022112009990589

Finnigan JJ (2000) Turbulence in Plant Canopies. Annual Review of Fluid Mechanics 32(1):519–571, DOI 10.1146/annurev.fluid.32.1.519

Freire LS, Chamecki M, Patton EG (2023) Atmospheric small-scale turbulence from three-dimensional hot-film data. Boundary-Layer Meteorology 189(1):77–101

Gao W, Shaw R, Paw U K (1989) Observation of organized structure in turbulent flow within and above a forest canopy. Boundary Layer Studies and Applications: A Special Issue of Boundary-Layer Meteorology in honor of Dr Hans A Panofsky (1917–1988) pp 349–377

Garratt J (1990) The internal boundary layer—A review. Boundary-layer meteorology 50:171–203

Ghisalberti M, Nepf HM (2002) Mixing layers and coherent structures in vegetated aquatic flows. Journal of Geophysical Research: Oceans 107(C2):3–1

Goldshmid RH, Winiarska E, Liberzon D (2022) Next generation combined sonic-hotfilm anemometer: wind alignment and automated calibration procedure using deep learning. Experiments in Fluids 63(1):30

Grant A (1991) Surface drag and turbulence over an inhomogeneous land surface. Boundary-layer meteorology 56:309–337

Hilel Goldshmid R, Liberzon D (2020) Obtaining turbulence statistics of thermally driven anabatic flow by sonic-hot-film combo anemometer. Environmental Fluid Mechanics 20(5):1221–1249

van Hout R, Zhu W, Luznik L, Katz J, Kleissl J, Parlange M (2007) Piv measurements in the atmospheric boundary layer within and above a mature corn canopy. part i: statistics and energy flux. Journal of the atmospheric sciences 64(8):2805–2824

Joshi P, Anderson W (2022) Surface layer response to heterogeneous tree canopy distributions: roughness regime regulates secondary flow polarity. Journal of Fluid Mechanics 946:A28, DOI 10.1017/jfm.2022.583

Kaimal JC, Finnigan JJ (1994) Atmospheric Boundary Layer Flows: Their Structure and Measurement. Oxford University Press, DOI 10.1093/oso/9780195062397.001.0001

Katul GG, Oren R, Manzoni S, Higgins C, Parlange MB (2012) Evapotranspiration: A process driving mass transport and energy exchange in the soil-plant-atmosphere-climate system. Reviews of Geophysics 50(3)

Kit E, Liberzon D (2016) 3D-calibration of three-and four-sensor hot-film probes based on collocated sonic using neural networks. Measurement Science and Technology 27(9):095,901

Kit E, Cherkassky A, Sant T, Fernando H (2010) In situ calibration of hot-film probes using a collocated sonic anemometer: implementation of a neural network. Journal of Atmospheric and Oceanic Technology 27(1):23–41

Kröniger K, De Roo F, Brugger P, Huq S, Banerjee T, Zinsser J, Rotenberg E, Yakir D, Rohatyn S, Mauder M (2018) Effect of secondary circulations on the surface–atmosphere exchange of energy at an isolated semi-arid forest. Boundary-Layer Meteorology 169:209–232

Li D, Huai W, Guo Y, Liu M (2022) Flow characteristics in partially vegetated channel with homogeneous and heterogeneous layouts. Environmental Science and Pollution Research 29(25):38,186–38,197, DOI 10.1007/s11356-021-18459-2

Mao RR, Lu Y, Cheng NS (2024) Experimental investigation of turbulent energy spectra affected by submerged vegetation in shallow open channel flows. Physics of Fluids 36(12)

Medjnoun T, Vanderwel C, Ganapathisubramani B (2018) Characteristics of turbulent boundary layers over smooth surfaces with spanwise heterogeneities. Journal of Fluid Mechanics 838:516–543, DOI 10.1017/jfm.2017.849

Moltchanov S, Bohbot-Raviv Y, Duman T, Shavit U (2015) Canopy edge flow: A momentum balance analysis. Water Resources Research 51(4):2081–2095

Nezu I, Onitsuka K (2002) PIV Measurements of side-cavity open-channel flows —Wando model in rivers—. Journal of Visualization 5(1):77–84, DOI 10.1007/BF03182606

Omidvar H, Bou-Zeid E, Li Q, Mellado JP, Klein P (2020) Plume or bubble? Mixed-convection flow regimes and city-scale circulations. Journal of Fluid Mechanics 897:A5

Patton EG, Sullivan PP, Shaw RH, Finnigan JJ, Weil JC (2016) Atmospheric stability influences on coupled boundary layer and canopy turbulence. Journal of the Atmospheric Sciences 73(4):1621–1647

Poggi D, Porporato A, Ridolfi L, Albertson J, Katul G (2004) The effect of vegetation density on canopy sub-layer turbulence. Boundary-Layer Meteorology 111:565–587

Pope SB (2001) Turbulent flows. Measurement Science and Technology 12(11):2020, DOI 10.1088/0957-0233/12/11/705

Raasch S, Harbusch G (2001) An analysis of secondary circulations and their effects caused by small-scale surface inhomogeneities using large-eddy simulation. Boundary-layer meteorology 101:31–59

Raupach M, Coppin P, Legg B (1986) Experiments on scalar dispersion within a model plant canopy part I: The turbulence structure. Boundary-Layer Meteorology 35:21–52

Raupach MR, Thom AS (1981) Turbulence in and above plant canopies. Annual review of fluid mechanics 13(1):97–129

Saddoughi SG, Veeravalli SV (1994) Local isotropy in turbulent boundary layers at high Reynolds number. Journal of Fluid Mechanics 268:333–372

Seginer I, Mulhearn P, Bradley E, Finnigan J (1976) Turbulent flow in a model plant canopy. Boundary-Layer Meteorology 10:423–453

Shaw R, Silversides R, Thurtell G (1974) Some observations of turbulence and turbulent transport within and above plant canopies. Boundary-Layer Meteorology 5:429–449

Thomas C, Foken T (2007) Flux contribution of coherent structures and its implications for the exchange of energy and matter in a tall spruce canopy. Boundary-Layer Meteorology 123:317–337

Unigarro Villota S, Ghisalberti M, Philip J, Branson P (2023) Characterizing the Three-Dimensional Flow in Partially Vegetated Channels. Water Resources Research 59(1):e2022WR032,570

Vanderwel C, Ganapathisubramani B (2015) Effects of spanwise spacing on large-scale secondary flows in rough-wall turbulent boundary layers. Journal of Fluid Mechanics 774:R2

Vanderwel C, Stroh A, Kriegseis J, Frohnapfel B, Ganapathisubramani B (2019) The instantaneous structure of secondary flows in turbulent boundary layers. Journal of Fluid Mechanics 862:845–870, DOI 10.1017/jfm.2018.955

White BL, Nepf HM (2008) A vortex-based model of velocity and shear stress in a partially vegetated shallow channel. Water Resources Research 44(1), DOI 10.1029/2006WR005651

Wilson JD, Ward DP, Thurtell GW, Kidd GE (1982) Statistics of atmospheric turbulence within and above a corn canopy. Boundary-Layer Meteorology 24(4):495–519, DOI 10.1007/BF00120736

Winiarska E, Soffer R, Klopfer H, van Hout R, Liberzon D (2023) The effects of spanwise canopy heterogeneity on the flow field and evaporation rates. Environmental Fluid Mechanics 23(6):1313–1339

Winiarska E, Liberzon D, van Hout R (2024) Flow field characteristics at the spanwise edge of a vegetative canopy model. Boundary-Layer Meteorology 190(10):40

Yan XF, Wai WHO, Li CW (2016) Characteristics of flow structure of free-surface flow in a partly obstructed open channel with vegetation patch. Environmental Fluid Mechanics 16(4):807–832, DOI 10.1007/s10652-016-9453-4

Zhu W, Van Hout R, Luznik L, Kang H, Katz J, Meneveau C (2006) A comparison of PIV measurements of canopy turbulence performed in the field and in a wind tunnel model. Experiments in fluids 41:309–318

Zhu W, van Hout R, Katz J (2007) On the flow structure and turbulence during sweep and ejection events in a wind-tunnel model canopy. Boundary-layer meteorology 124:205–233